Journal of Petrology, 2017, Vol. 58, No. 5, 841–862 doi: 10.1093/petrology/egx036 Advance Access Publication Date: 4 August 2017 Original Article



Understanding Degassing and Transport of CO₂-rich Alkalic Magmas at Ross Island, Antarctica using Olivine-Hosted Melt Inclusions

Daniel J. Rasmussen^{1,2}*, Philip R. Kyle¹, Paul J. Wallace³, Kenneth W. W. Sims⁴, Glenn A. Gaetani⁵ and Erin H. Phillips⁴

¹Department of Earth and Environmental Science, New Mexico Institute of Mining and Technology, Socorro, NM 87801, USA; ²Department of Earth and Environmental Sciences, Lamont–Doherty Earth Observatory of Columbia University, Palisades, NY 10964, USA; ³Department of Earth Sciences, University of Oregon, Eugene, OR 97403, USA; ⁴Department of Geology and Geophysics, University of Wyoming, Laramie, WY 82071, USA; and ⁵Department of Geology and Geophysics, Woods Hole Oceanographic Institution, Woods Hole, MA 02543, USA

*Corresponding author. Telephone: 845-365-8454. Fax: 845-365-8155. E-mail: danielr@ldeo.columbia.edu Received March 7, 2016; Accepted June 5, 2017

ABSTRACT

Volatiles play an important role in magmatic and volcanic processes. Melt inclusions are a powerful tool to study pre-eruptive volatiles, but interpretation of their H₂O and CO₂ variations can be difficult. The H₂O and CO₂ contents of melt inclusions from nine basanites from Hut Point Peninsula, Mt Terror and Mt Bird on Ross Island, Antarctica, were studied to understand better the behavior of volatiles in the magmas and to provide insight into magma transport and storage processes. Ninety olivine-hosted (Fo78-88) melt inclusions were examined along with the composition of the associated bulk-rock samples. The H₂O (0.4-2.0 wt %) and CO₂ (0.2-0.9 wt %, or 0.2-1.8 wt % after correction for vapor bubbles) variations in the melt inclusions cannot be explained by equilibrium degassing. A strong correlation between melt inclusion radius and H₂O content for Hut Point samples indicates that diffusive loss of H⁺ has occurred. Based on vapor saturation pressure trends, it is inferred that a magma reservoir existed below Hut Point at a depth of ~18 km, and by modeling diffusive loss of H+ for melt inclusions, it is shown that the magmas ascended from this depth in less than a year. Melt inclusions from Terror and Bird lack evidence of diffusive loss of H⁺ and there are no strong chemical indicators of CO2 fluxing. Compositional heterogeneities in melt inclusions indicate that magma mixing occurred, making it difficult to interpret H2O and CO2 trends. Melt inclusions from these volcanoes were entrapped polybarically, inconsistent with entrapment in a single storage region. Published analyses of 54 olivine-hosted (Fo53-83) melt inclusions in seven samples from Erebus volcano on Ross Island were re-examined for comparative purposes. Low H₂O (~0.1 wt %) and CO₂ (0-0.2 wt %) contents and the evolved compositions of these indicate that Erebus magmas undergo shallow (<6km) crystallization before eruption, probably in a shallow storage region. Magmas from the surrounding volcanoes show no sign of shallow storage.

Key words: alkali basalt; melt inclusion; Polar Rock Repository; Ross Island; volatile; degassing; magma ascent; magma chamber; diffusion modeling; olivine

INTRODUCTION

Studies of magmatic volatiles offer insight into melt generation, magma transport and evolution, and global volatile cycles (e.g. Grove & Baker, 1984; Allard *et al.*,

1991; Gaetani & Grove, 1998; Dixon *et al.*, 2002; Wallace, 2005). Such efforts require knowledge of the behavior of volatiles in the pre-eruptive magmas, which is a challenge because magmas degas during their

ascent to the surface and retain only a small fraction of their initial volatile contents after eruption. The direct measurement of pre-eruptive volatile concentrations is possible through the study of glass inclusions, known as melt inclusions (MIs). These small (tens of microns) blebs of silicate glass represent melt entrapped in growing crystals during various stages of magma ascent and differentiation, thereby providing a window into the changing physicochemical states of magmas prior to their eruption.

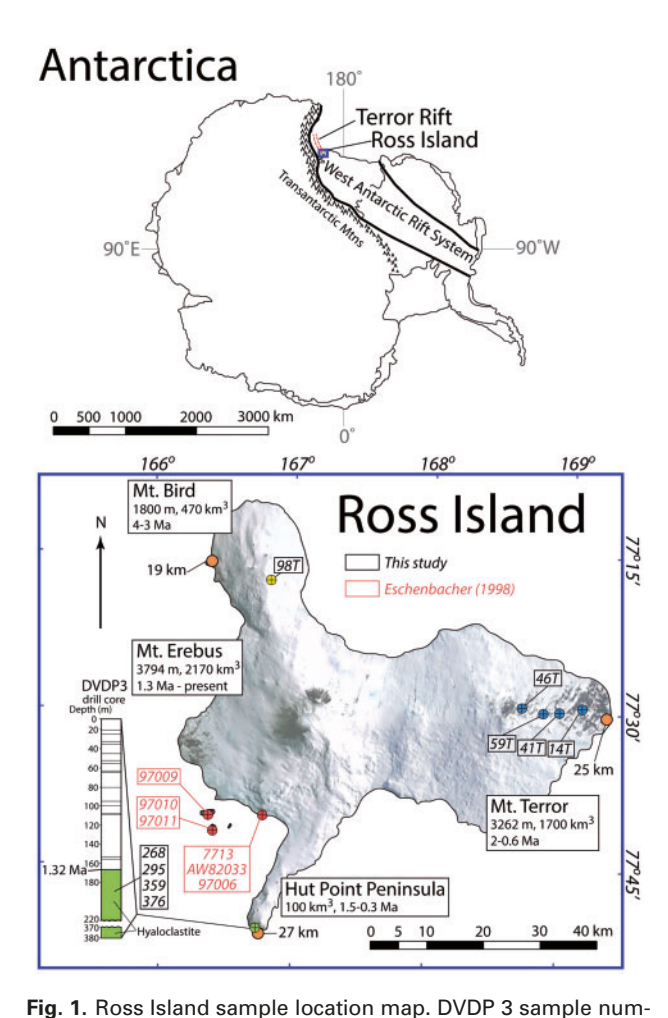
One important goal of MI studies is to elucidate magmatic degassing processes, which may be reflected in the compositions of polybarically entrapped MIs (Wallace, 2005), provided that proper consideration is given to post-entrapment cooling and bubble growth (Steele-MacInnis et al., 2011). Mafic magmas are often considered to follow equilibrium degassing paths (Sparks et al., 1994), which are predicted using models (Newman & Lowenstern, 2002; Papale et al., 2006) and decompression experiments (Lesne et al., 2011). Interestingly, MIs often show variations in H₂O and CO₂ contents that are inconsistent with model predictions (Blundy et al., 2010). The inconsistency is most commonly attributed to processes that affected the magma prior to MI entrapment. Studies often invoke CO2 fluxing, or buffering of magmatic volatiles by the addition of a CO₂-rich vapor. Disequilibrium degassing has also been suggested (e.g. Gonnermann & Manga, 2005; Pichavant et al., 2013). Recent efforts have underscored the importance of MI-specific mechanisms in causing the inconsistency, such as post-entrapment diffusive loss of H⁺ (e.g. Gaetani et al., 2012; Bucholz et al., 2013; Mironov et al., 2015). Most investigations of the enigmatic H₂O and CO₂ behavior have focused on H₂O-rich arc magmas and/or evolved magma compositions, whereas studies of primitive alkalic systems have been mostly confined to Mt Etna (e.g. Métrich & Clocchiatti, 1989; Spilliaert et al., 2006; Collins et al., 2009). Alkalic magmas provide a critical test for CO₂-fluxing because they typically have high magmatic CO2 concentrations, inherited from their generation by low degrees of partial melting and possible enriched mantle sources (Sun & McDonough, 1989; Dasgupta et al., 2007).

We report volatile, major and trace element concentrations in olivine-hosted MIs from basanitic tephras and hyaloclastites from Ross Island, Antarctica. Our aim is to understand the behavior of H₂O and CO₂ through studying variations recorded in Mls. These variations are used to investigate ascent timescales and depths of crystallization and mixing. Previous studies of MIs from Ross Island focused on evolved magmas from Erebus and demonstrated the CO₂-rich nature of the magmas and the deviation of H₂O and CO₂ contents from equilibrium degassing paths (Eschenbacher, 1998; Oppenheimer et al., 2011). This study focuses on basanites from Hut Point Peninsula, Mt Terror, and Mt Bird. The new results are compared with the published data from Erebus to evaluate the plumbing system and distribution of volatiles in magmas at Ross Island.

GEOLOGICAL SETTING

Ross Island (Fig. 1) is an alkalic volcanic center located within the West Antarctic Rift System, a broad region of thinned Antarctic continental crust characterized by extension, high heat flow, and volcanism (Behrendt, 1999). North of Ross Island is the Terror Rift, where extension in the West Antarctic Rift System has been focused from the late Miocene to the present (Hall *et al.*, 2007). Finotello *et al.* (2011) used receiver functions to determine crustal thicknesses of 19–27 km below Ross Island (Fig. 1), similar to \sim 18–25 km crustal thicknesses within the Terror Rift (Watson *et al.*, 2006). Magmatic activity is typically attributed to extensional tectonics (e.g. Rocchi *et al.*, 2005; Cooper *et al.*, 2007) or upwelling of deep mantle (e.g. Kyle *et al.*, 1992; Sims *et al.*, 2008; Gupta *et al.*, 2009).

Over the last \sim 4 Myr, eruptions of \sim 4520 km³ of basanite to phonolite, with minor benmoreite and trachyte,



bers correspond to sample location map. DVDP 3 sample numbers correspond to sample depths (in m) in the core. Crustal thicknesses (orange circles) are from Finotello *et al.* (2011). Volumes and ages of the four volcanic centers are from Kyle (1990*a*) and Esser *et al.* (2004), and the age of the top of the hyaloclastite unit in DVDP 3 is inferred from a correlative unit in DVDP 2 (Kyle *et al.*, 1981*a*). Samples from Erebus, which include samples from a sea cliff and outlying islands, are those of Eschenbacher (1998). The Antarctica base map and image of Ross Island are courtesy of the U. S. Geological Survey.

have built the four coalesced volcanic centers that form Ross Island-Mount Bird, Mount Terror, Hut Point Peninsula, and Mount Erebus-which are hereafter referred to as Bird, Terror, Hut Point, and Erebus (Armstrong, 1978; Kyle et al., 1992; Esser et al., 2004). Volcanism began at Bird, lasting from ~4 to 3 Ma (Kyle, 1990b). Mostly basanitic eruptions formed the 1800 m high shield volcano, which has parasitic basanitic and phonolitic scoria cones populating its flanks (Wright & Kyle, 1990a). Volcanism at Terror (3230 m) occurred from 2 to ~ 0.6 Ma (Kyle, 1990a), forming a mafic shield volcano (Wright & Kyle, 1990b). Numerous basanitic cones and phonolite domes are scattered about the flanks. Hut Point volcanism spanned ~1.5-0.3 Ma (Kyle, 1990a). Hut Point is a 20 km long, 2-4 km wide line of mostly basanitic scoria cones and lavas with a 228 m tall endogenous phonolite dome near its southern terminus (Kyle, 1990b), Erebus, the only active volcano on Ross Island, has had three phases of construction (Esser et al., 2004). Mafic eruptions from 1.3 to 1.0 Ma built the proto-Erebus shield. A cone building phase, distinguished by eruptions of evolved phonotephrites and tephriphonolites, followed from ~ 1.0 to $0.25\,\mathrm{Ma}$. Most of the modern edifice formed since 250 ka with the eruption of tephriphonolite to phonolite lava flows and minor pyroclastic material. Englacial tephra deposits in the East Antarctic ice sheet provide evidence of at least two large, possibly Plinian, eruptions at Erebus (Harpel et al., 2008; Iverson et al., 2014). No large-scale explosive eruptions have been attributed to Hut Point, Terror, or Bird.

SAMPLES

The studied suite includes nine basanite samples: four rapidly quenched marine hyaloclastites from Hut Point, four tephras from Terror, and one tephra from Bird (Fig. 1). The Hut Point hyaloclastite samples were cored during the Dry Valley Drilling Project (DVDP) in 1973. We examined MI samples from 268, 295, 359, and 376 m depths of DVDP hole 3, all part of a 214 m thick basanitic hyaloclastite consisting of palagonitic tuffs and breccias with interspersed pillow fragments (Kyle, 1981a). Olivine was sampled from the palagonitic matrix. To characterize the host magmas from which the MIs formed, pillow fragments were sampled nearest the depths from which the MI samples came (267-38, 306-33, 359-02, and 376-85 m). Mafic lapilli tuffs and tuff breccias were collected from scoria cones on Terror (14T, 41T, 46T, 59T) and Bird (98T). Loose olivine was picked from the ash size fraction. In situ bombs and blocks from agglutinates and lava flow samples were collected near the sampled tephra deposits. These samples, along with fresh lapilli clasts from the tephras, were used to examine the host magma. Further descriptions of the samples can be found in Supplementary Data Electronic Appendix 1 (supplementary data are available for downloading at http://www.petrology. oxfordjournals.org).

ANALYTICAL METHODS

Analytical methods summarized here are detailed in Supplementary Data Electronic Appendix 2.

Major and trace element analyses of bulk samples

A total of 37 samples of fresh lapilli clasts from tephra, pillow fragments in hyaloclastites and lavas or agglutinates were crushed in a quartz swing mill. They were analyzed for bulk-rock major element and Sr concentrations at Michigan State University using a Bruker S4 PIONEER wavelength-dispersive X-ray fluorescence (XRF) spectrometer; trace element contents were measured by inductively coupled plasma mass spectrometry (ICP-MS) on a Thermo Scientific ICAP Q quadrupole ICP-MS system connected to a Photon Machines G2 193 nm excimer laser ablation system. Analytical methods followed those of Rooney et al. (2012). Replicate analyses of BHVO-1, used as a check standard, have precisions (1 σ) of <0.4% for all elements except P₂O₅, for which precision was 3.6%. For trace element analyses, JB-1 a and BHVO standards were measured to assess analytical precision. Reproducibility was <1% for Sc, Ni, Rb, Zr, Ba, La, and Ce; <3% for V, Cr, Co, Y, Nb, Cs, Pr, Eu, Gd, Tb, Ho, Er, Yb, Lu, Ta, Pb, Th, and U; and <4% for Nd, Sm, Dy, Tm, and Hf.

Mineral and glass analyses

Mineral and glass analyses were obtained from 90 doubly polished olivine-hosted Mls, 29 matrix glasses, and 268 minerals (olivine, pyroxene, kaersutite, spinel, feldspar, apatite, leucite).

Fourier transform infrared spectroscopy

FTIR spectroscopy was performed on 82 MIs at the University of Oregon using a Thermo-Nicolet Nexus 670 FTIR spectrometer interfaced with a Continuum IR microscope. Quantitative measurements of H₂O and CO₂ (as CO₃²⁻) were obtained by measuring absorbance spectra with 120-150 scans between 4000 and 1000 cm⁻¹. In most cases, three replicate spectra were collected on each MI. Vapor bubbles, when present, were avoided using the masking aperture in the FTIR system. A single absorbance spectrum of each host olivine was collected and compared with the MI spectra to check for incomplete intersection of the MI. For six MIs (41 T-21, 59 T-9, 59 T-29, 59 T-31, 359-8, 359-10) that were incompletely intersected, the maximum peak height of second-order Si-O overtones occurring between 1600 and 2100 cm⁻¹, which corresponds to olivine in the FTIR spectra, was measured on both host and MI spectra, and a ratio of the two was used to correct (by reducing) the thickness of each inclusion used in the Beer-Lambert calculation. We obtained three reflectance spectra of the host to calculate wafer thickness, following the method of Wysoczanski & Tani (2006). Total H₂O and CO₂ concentrations were calculated using the Beer-Lambert law with a value of 63 L

mol $^{-1}$ cm $^{-1}$ for ϵ_{3520} (total $H_2O)$ (Dixon $\it{et~al.}$, 1997) and the compositionally dependent model of Mandeville $\it{et~al.}$ (2002) for ϵ_{1430} and ϵ_{1515} (carbonate). Analyzed MIs were 13–69 μm thick. Measured H_2O and CO_2 concentrations have precisions (1 σ) of <10% and <12%, respectively, which include uncertainties in glass thickness, density, and absorbance.

Electron microprobe analysis

All 90 Mls and their host olivines were analyzed for their major element and S, Cl, and F compositions using a CAMECA SX-100 electron microprobe in a single session at the CAMCOR facility, University of Oregon. Generally, three replicate analyses were performed on each Ml and each olivine crystal. Spot analyses of Mls did not overlap and were performed near their centers. Olivine analyses were conducted within no more than a few tens of micrometers of the Ml but no less than 5–10 μm .

Glasses were analyzed using a 10 µm beam diameter, 15 kV accelerating voltage and 10 nA for K (80 s), Al (80 s), Na (80 s), Si (80 s), Mg (80 s), Ca (80 s), S (80 s), and Fe (150 s), and 50 nA current for Mn (90 s), S (80 s), CI (120 s), Ti (100 s), P (160 s), and F (160 s). Si, Fe, Mg, and Ca in olivine were analyzed with a 10 µm diameter beam, 15 kV accelerating voltage, 30 nA current and a count time of 80 s for all elements. Synthetic and natural minerals, oxides, and glasses were used as calibration standards and were analyzed twice to monitor instrument drift over time. Data were reduced using Probe for EPMA 10.0.7 software. Si, Al, Na, and K were corrected for the effects of alkali migration (Humphreys et al., 2006) by extrapolating intensity-time plots to time zero. A fixed value of 1 wt % H₂O was used for the matrix correction of all Mls. Replicate glass analyses of unknowns have averaged precisions (1 σ) of $\leq 3.5\%$ for SiO₂, TiO₂, Al_2O_3 , FeO, MgO, CaO, Na₂O, K₂O, P₂O₅, S, and Cl, and <9.5% for MnO and F.

Matrix glass and non-host minerals were analyzed and imaged on a Cameca SX-100 at New Mexico Tech. The analytical conditions and precision are provided in Supplementary Data Electronic Appendix 2.

Laser ablation ICP-MS of MIs

Trace element abundances were measured in 81 MIs using a Photon Machines G2 short pulse length 193 nm ArF Excimer laser coupled to a Thermo Xseries2 quadrupole ICP-MS system at the W. M. Keck Collaboratory for Plasma Spectrometry, Oregon State University (see Kent et al., 2004). Helium was used as the carrier gas. A beam diameter of 40 µm or (rarely) 30 µm was used with a pulse frequency of 7 Hz and shot count of 225. Special care was taken to avoid analyzing crystal inclusions in MIs. The USGS GSE-1G glass was measured as a calibration standard and USGS glass standards BHVO-2G and BCR-2G were measured to estimate accuracy and precision. Elemental concentrations were determined using Ca as an internal standard with abundances being

those obtained from electron microprobe analyses (corrected for post-entrapment processes, as described below). Precisions (1σ), which include uncertainty in calibration and internal standard measurements, are \leq 5% for Sc, Rb, Sr, Ba, La, Ce, Nd, and Sm; \leq 10% for V, Zn, Y, Zr, Gd, Dy, Yb, Hf, Pb, and Th; \leq 16% for Li, Ni, Cu, Nb, Er, and U; and \leq 23% for Cr and Cs.

CORRECTION OF MI DATA FOR POST-ENTRAPMENT PROCESSES

Post-entrapment crystallization and diffusive Fe-Mg exchange

Post-entrapment crystallization (PEC) of olivine along the MI–host interface is common in natural MI suites, but the effects of this process are often difficult to discern optically (Kent, 2008). PEC has the effect of depleting elements compatible in olivine and enriching those that are incompatible. A secondary result of PEC is disequilibrium between the host, PEC rind, and MI, which can result in diffusive Fe–Mg exchange between the MI and host (Danyushevsky et al., 2000; Gaetani & Watson, 2000). Although the effects of PEC are most pronounced near the melt–olivine interface, in many cases the center may be affected as well (Newcombe et al., 2014), so positioning analyses near the center of the MI reduces, but often fails to eliminate, the effects of PEC.

The effects of PEC were examined by comparing the measured host Fo with a predicted equilibrium olivine Fo content, calculated using the measured MI composition and appropriate values for Fe redox state and Fe²⁺-Mg partitioning (K_D). The ferric-ferrous ratio was estimated using the model of Kress & Carmichael (1991) and assuming oxygen fugacity on the quartzfayalite-magnetite (QFM) buffer, which is appropriate for magmas from Erebus (Kyle, 1977; Kyle et al., 1992) and in the range for global mid-ocean ridge basalt (MORB) (Cottrell & Kelley, 2011) and ocean island basalt (OIB) (Mallmann et al., 2011). Using the olivine-melt model proposed by Danyushevsky (2001), calculated K_D values are 0.29 ± 0.01 . In most cases, MIs examined in the present study are in equilibrium with a lower Fo olivine than the host, indicating that PEC has occurred, which is reflected in lower than expected concentrations of MgO (Fig. 2a). Diffusive Fe²⁺ exchange was assessed by comparing MI and bulk-rock FeOt values. At the same extent of differentiation, FeO_t concentrations of the MIs are lower than bulk-rock values (Fig. 2b), which is consistent with diffusive loss of Fe2+ from the MIs.

MI major and volatile element compositions were corrected for the effects of PEC and diffusive Fe–Mg exchange using the Petrolog3 software (Danyushevsky & Plechov, 2011). The FeO_t contents of MIs were assumed to fall on a liquid line of descent defined by a polynomial regression of the bulk-rock data (Fig. 2b). This type of Fe correction is an oversimplification because it relies on the assumption that the bulk-rock composition is indicative of the melt originally entrapped to form the MI.

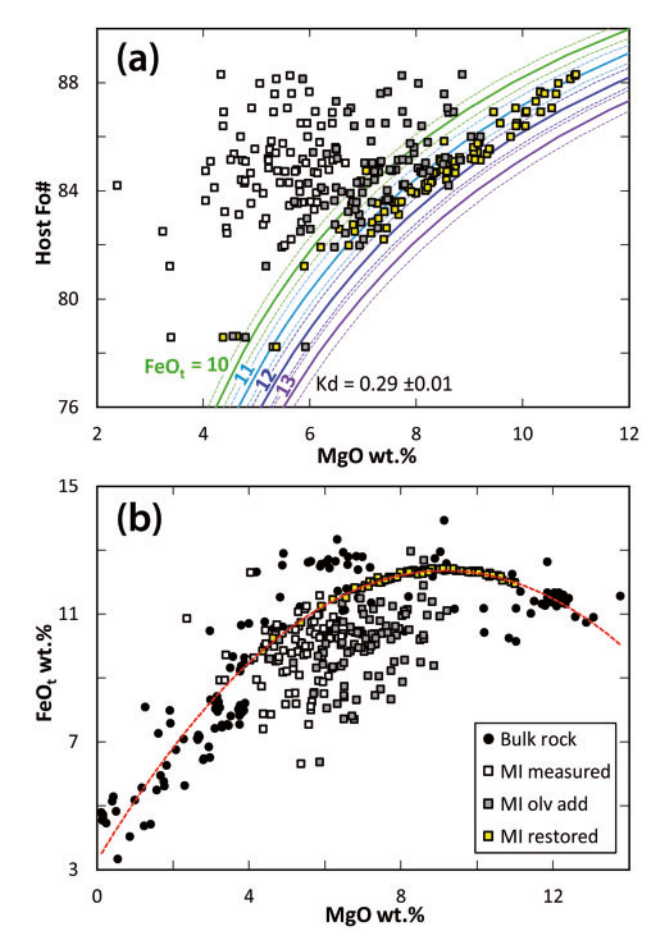


Fig. 2. Plots of olivine host composition (a) and bulk-rock and melt inclusion (MI) FeO_t content (b) vs MgO content for Ross Island, illustrating the effects of post-entrapment modification of Mls. Originally measured, olivine addition and restored compositions are all shown for Mls. (a) Comparison of host olivine compositions with MgO content of Mls, which indicates that most MIs have compositions that fall below the equilibrium line for appropriate values of FeO_t and K_d . (b) Total iron as FeO(FeO_t) vs MgO content for MIs and bulk-rock samples, showing that most uncorrected MI compositions and MI compositions with olivine addition (and no Fe correction) fall below the FeO_t of the liquid line of descent, consistent with diffusive loss of Fe²⁺ from Mls. The red dashed line is a polynomial regression of the bulk-rock data, which was used to infer the original FeOt of the Mls. Data from this study (Supplementary Data Table EA3.12), Cole & Ewart (1968), Goldich et al. (1975), Kyle (1976, 1981b) and Stuckless et al. (1981). Compiled data are reported in Supplementary Data Table EA3.14.

However, the effect of the correction on most elements, apart from MgO and FeO_t, is relatively minor, and corrected MI compositions better coincide with bulk-rock and modeled evolutionary trends (Figs 2–4).

In the present study, PEC corrections require olivine additions of up to $21.9\,\mathrm{wt}$ % (average $11.8\,\mathrm{wt}$ %) and the difference between measured FeO_t and the final, corrected FeO_t is as much as $5.6\,\mathrm{wt}$ % (average $2.4\,\mathrm{wt}$ %). Subtraction of olivine is required for one MI (98T-4), which needed $0.4\,\mathrm{wt}$ % olivine subtracted. There were two MIs (14T-1 and 98T-4) that require the removal of FeO_t, meaning the PEC corrected MI compositions fell above the bulk-rock value of FeO_t. These corrections are

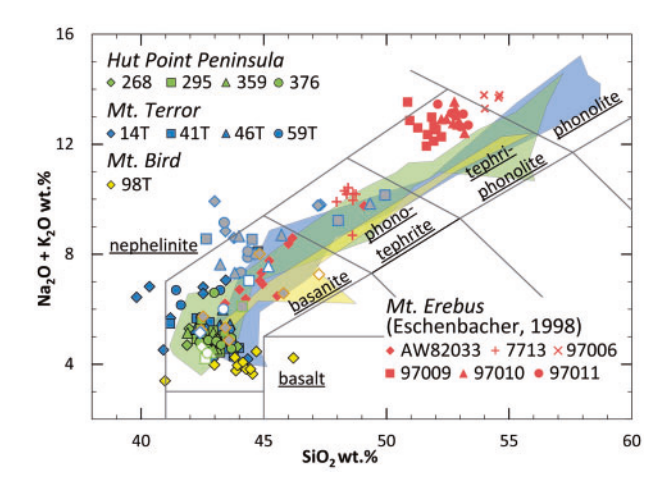


Fig. 3. Total alkalis–silica diagram for melt inclusions (MIs) from Ross Island, matrix glasses (gray fill), and bulk-rocks associated with MI samples (white fill). All compositions are normalized to 100% and volatile-free. Bulk-rock arrays from Bird, Terror, and Hut Point are overlapping and MI compositions occupy the least evolved end of the array. Erebus MIs are from Eschenbacher (1998). Fields are whole-rock analyses from Hut Point (green), Terror (blue), and Bird (yellow), which include the same data as in Fig. 2.

minor, requiring subtractions of 0.4 and 0.3 wt %, respectively.

The MI compositions reported here have been corrected for PEC and Fe–Mg exchange. MI compositions from Eschenbacher (1998) were also corrected for the effects of PEC and Fe–Mg exchange using the same methods as described above. Uncorrected analytical results of MIs from this study are given in Supplementary Data Electronic Appendix 3 Table EA3.1, and restored compositions of MIs from this study and Eschenbacher (1998) are given in Electronic Appendix 3 Table EA3.2 and EA3.3, respectively.

Vapor bubble formation

Vapor bubbles are common in Mls (Lowenstern, 1995). They form through a combination of PEC, which results in a net volume decrease, and melt contraction caused by cooling, which is due to the greater thermal expansion of the melt compared with olivine (Roedder, 1979; Lowenstern, 1995; Wallace et al., 2015). These effects cause a pressure drop inside MIs that results in nucleation and growth of a vapor bubble. Diffusive loss of H⁺ is also likely to play a role in vapor bubble formation and growth (Bucholz et al., 2013). Decompression of the external melt has been shown to have relatively minor effects on the internal pressure of the MI (Tait, 1992). In most cases when vapor bubble growth occurs, the largest effect on the melt is decreased dissolved CO2 concentration (Steele-MacInnis et al., 2011; Moore et al., 2015), owing to its low solubility relative to other major volatile species (H₂O, S, Cl, F).

All but eight MIs contain vapor bubbles. The number (0–4) and size (9–59 μ m diameter, 21 μ m average) of the bubbles is variable. The vapor bubbles occupy 1–22 vol. % of the MI (Supplementary Data Table EA3.4);

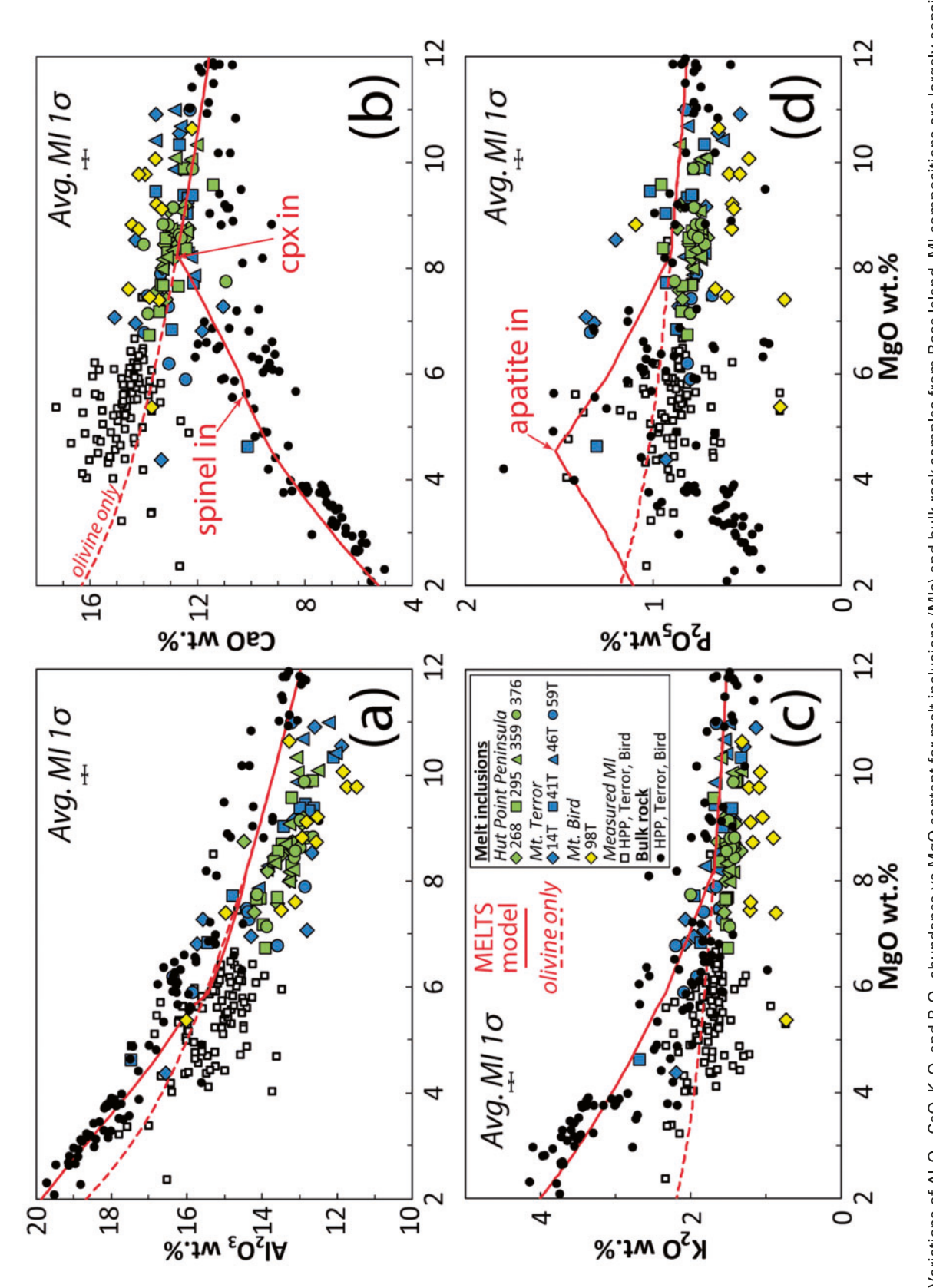


Fig. 4. Variations of Al₂O₃, CaO, K₂O, and P₂O₅ abundance vs MgO content for melt inclusions (Mls) and bulk-rock samples from Ross Island. MI compositions are largely consistent with olivine-only fractionation. Mls have slightly high values of CaO and lower values of Al₂O₃ relative to measured bulk-rock compositions. Lines are modeled fractional crystallization paths obtained using MELTS (Ghiorso & Sack, 1995), with DVDP2-105.53 as the starting melt composition (Kyle, 1981*b*). The conditions of the calculation are given in Supplementary Data 2. The dashed path is olivine-only fractionation. Bulk-rock data are the same as in Fig. 2.

these volumes were estimated assuming ellipsoid and sphere geometries for Mls and vapor bubbles, respectively, with the third axis (not viewable in prepared Ml wafers) assumed to be equal to the length of the shorter measured axis. Vapor bubbles that are $<\sim 3-5$ vol. % of the Ml are likely to have formed by shrinkage (Moore et al., 2015; Wallace et al., 2015). Larger bubbles are probably due to the co-entrapment of an exsolved vapor phase with the Ml (Wallace et al., 2015; Aster et al., 2016), which is consistent with the highly variable volume per cent of vapor bubbles. Variable extents of post-entrapment diffusive H⁺ loss, inferred from H₂O/Ce in relation to Ml size and location (see section below), are also likely to have played a role in the wide size range of bubbles (Bucholz et al., 2013).

The effects of vapor bubble growth have been evaluated by using the computational approach of Wallace et al. (2015), which assumes MI shrinkage to be due to the combined effects of cooling and crystallization. To perform the calculation, the pre-eruptive vapor bubble volume percentage was estimated by the method of Riker (2005), which is based on phase equilibria and the densities and coefficients of thermal expansion for tholeiitic melts and olivine. Temperature estimates for the pre-eruptive MIs were calculated using the measured MI compositions. Original trapping temperatures were determined using the PEC/Fe-loss corrected MI compositions. For both, we used equation (4) of Putirka et al. (2007). The measured volume of the MI was then used to determine the pre-eruptive volume of the vapor bubble. The moles of CO₂ in the bubble were calculated using the Redlich-Kwong equation of state with the bubble volume, modeled pressure, mole fraction of CO₂ in the vapor phase [calculated using the method of Newman & Lowenstern (2002)], and temperature. The vapor phase was calculated to be dominantly CO₂ (>85 mol % in nearly all cases). The effect of vapor bubble formation on H₂O is assumed to be negligible. Vapor bubbles were found to contain 3-55% (average 36%) of the total CO2. Uncertainties in the estimated initial CO2 concentrations are based on the error contributed from both the FTIR measurements and vapor bubble addition, which is based on error introduced by the thermometry.

RESULTS

Rock textures and mineral assemblages

Rock textures described here are discussed further in Supplementary Data Electronic Appendix 1. Mineral analyses are reported in Electronic Appendix 3 Tables EA3.5–3.9.

All the Hut Point samples exhibit similar textures and mineral assemblages. Olivine (Fo_{75-90}) is euhedral and generally abundant ($\sim 10 \, \text{vol.}$ %). No other macrocryst phases are present. However, there is microlitic augite and plagioclase feldspar in the groundmass.

Samples from Terror and Bird have similar phenocryst assemblages and disequilibrium textures; rare

xenocrysts are present. Olivine (mostly Fo₇₂₋₉₀) is common (<14vol. %) and variably resorbed. There are rare grains of high-Fo olivine (\geq Fo₉₀) that are large (>3 mm), highly fractured, and partially dissolved. These grains have anomalously low CaO concentrations (0.07-0.20 wt %), indicating that they are likely to be of higher pressure origin (e.g. Larsen & Pedersen, 2000). Kaersutite is less common (≤7 vol. %). Most grains are reversely zoned, with rims \sim 20–270 μ m thick observed in backscattered electron (BSE) images; the cores are commonly rounded (Supplementary Data Fig. EA5.1), implying that magma mixing has occurred. Clinopyroxene, orthopyroxene, plagioclase feldspar and alkali feldspar are also present, showing varying degrees of zonation and dissolution textures. Orthopyroxene is likely to be xenocrystic because it is not an expected crystallizing phase in silicaundersaturated, alkalic rocks (Miyashiro, 1978).

Melt inclusions

Melt inclusion morphologies

MI and host olivine morphological data and photomicrographs are reported in Supplementary Data Electronic Appendix 3 Table EA3.4 and Electronic Appendix 4, respectively. The MIs are fully enclosed and naturally glassy. Diameters of MIs range from 26 to 131 μm (average 61 μm). Of the 90 analyzed MIs, 35 contain crystal inclusions. In most cases, the crystals are of spinel and they are located at the MI–host interface. MIs with mineral inclusions are not outliers on compositional plots apart from a single MI from 376 (e.g. Figs 3 and 4). It is therefore unlikely that the mineral inclusions are daughter minerals crystallized from trapped melt. They are instead more likely to have been co-entrapped with melt as part of the process of MI formation (Roedder, 1979).

Olivine hosts of MIs

All MI-bearing olivines are euhedral and mostly free of matrix glass. Most have polyhedral morphology and contain spinel inclusions. During microprobe analysis, we observed no compositional zonation in BSE images. Olivines range in diameter from 0·4 to 1·9 mm (average 0·94 mm) and have overlapping compositions of Fo_{78–88}, with most between Fo₈₂ and Fo₈₈ (Fig. 2a). Olivine hosts have CaO concentrations of 0·22–0·38 wt % (Supplementary Data Table EA3.10), indicating that none belong to the high-Fo, low-CaO olivine population discussed above.

Major element compositions of MIs

When evaluating the compositions of MIs it is important to consider the possibility of boundary layer enrichment or depletion during trapping, which occurs when melt adjacent to a growing crystal becomes enriched in incompatible elements and depleted in compatible elements prior to entrapment (Faure & Schiano, 2005; Kent, 2008). This process is important when the crystal growth rate outpaces the diffusion of chemical species

into and out of the boundary layer melt. Boundary layer entrapment is unlikely to be important for our samples because we know of no natural datasets that show this process and Mls in hosts with slow growth morphologies were intentionally selected, although we do note that inferences of crystal growth rate based on morphology have recently been called into question (e.g. Welsch *et al.*, 2014). Additionally, slowly diffusing chemical species (e.g. P₂O₅) are not well correlated with melt inclusion size, which would occur during the entrapment of boundary layers because larger Mls are expected to be less affected by boundary layer processes.

Major element and volatile compositions of Mls, corrected for post-entrapment effects and normalized to 100%, are presented in Supplementary Data Electronic Appendix 3 Table EA3.2, along with the modeling results. Matrix glass and bulk-rock analyses are given in Electronic Appendix 3, Tables EA3.11 and EA3.12, respectively. Silica (39.0-45.4 wt %) and alkali (Na₂O + K₂O; 3·3–8·0 wt %) contents of MIs indicate that nearly all have basanite compositions (Fig. 3). MI compositions plot at the least evolved end of bulk-rock and matrix glass compositional arrays. The Hut Point MIs exhibit remarkably minor chemical variation despite spanning 108 m of the basanite hyaloclastite unit. Bulk tephra (and bulk-rock samples from the vicinity of MI-bearing tephras) have compositions that are relatively less (Hut Point samples, 14T, and 59T) or more (Terror, except 14T and 59T, and Bird samples) evolved than the associated MI compositions. The latter relationship is inconsistent with a simple model in which MIs formed from a parental melt, represented by the bulk-rock, which ascended in a closed system. It is much more likely that these samples were affected by open-system processes, including the addition of MI-bearing olivines to an evolved melt or mixing between more and less evolved magmas.

MI major element trends are broadly consistent with olivine crystallization and inconsistent with significant crystallization of the other observed macrocryst phases (e.g. clinopyroxene, kaersutite, feldspars, apatite; Fig. 4). Small yet distinct differences are exhibited in the behavior of major elements at each volcano. Olivine is the most abundant macrocryst phase in the Hut Point samples and MI compositions lie near the olivine-only fractional crystallization path, although bulk-rock trends appear to show clearly the effect of clinopyroxene fractionation (e.g. Fig. 4b). Terror MI compositions follow evolutionary trends similar to those from Hut Point, but the Terror MI compositions show greater scatter and some may reflect clinopyroxene fractionation (Fig. 4b-d). The Bird sample (98T) has MIs with compositions that are also generally consistent with olivine-only fractionation, although there are two MIs (98 T-4 and 98 T-12) with low values of K2O and P₂O₅ (Fig. 4c and d). These MIs also have trace element compositions that are anomalous, and they are interpreted to have a different origin.

When compared with the bulk-rock compositional array, MI compositions tend to plot at low values of Al₂O₃ and high values of CaO. Anomalous compositions

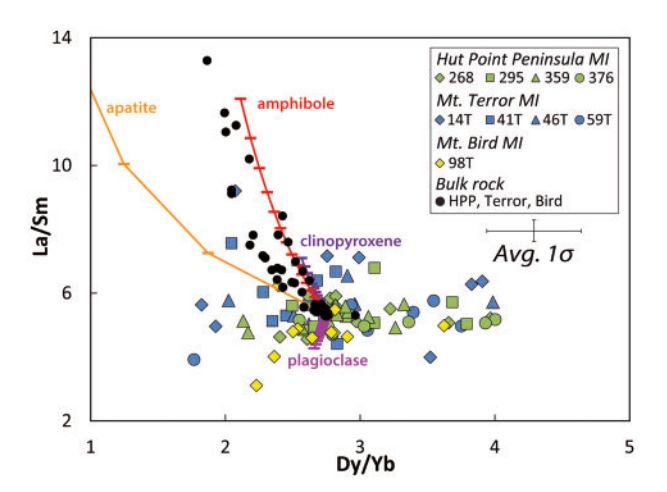


Fig. 5. La/Sm vs Dy/Yb for melt inclusions (MIs) and bulk-rock samples from Ross Island, showing that MI compositions have significant scatter in Dy/Yb. Each line shows a liquid line of descent that starts with the composition of DVDP2-105.53, a representative parental melt (Kyle, 1981b) undergoing fractional crystallization of the labeled phase. The ticks show 5 wt % crystallization increments. Mineral—melt partition coefficients used in the models are from McKenzie & O'Nions (1991).

such as these have been previously observed for MIs hosted in high-Fo olivines (e.g. Schiano *et al.*, 2000; Danyushevsky *et al.*, 2004). A thorough examination of the origin of high-Ca MIs is beyond the scope of this work, but there would appear to be two possible explanations. First, MIs may be related to a parental melt composition different from that from which the bulk-rock samples were derived. Second, the melts trapped as MIs may have been modified by grain-scale clinopyroxene assimilation (Danyushevsky *et al.*, 2004).

Trace element compositions of MIs

Trace element compositions of MIs are reported in Supplementary Data Electronic Appendix 3, Table EA3. 13. The MI trace element patterns are broadly consistent with those of the bulk-rock samples (i.e. chondritenormalized rare earth element patterns are similar; Fig. EA5.2). Additionally, MI and bulk-rock compositions have similar ratios of trace elements with similar partitioning (Fig. EA5.3). Kyle (1981b) investigated samples from the DVDP cores and suggested that the compositions are consistent with descent from a single parent with a composition of DVDP2-105.53. The MIs show significant scatter in trace element concentrations, which is less apparent in the bulk-rock samples (Fig. 5). Some of the variation in MI trace element composition may be due to crystal fractionation (e.g. La/Sm; Fig. 5), but other variation (e.g. Dy/Yb) cannot be explained in this way. It should be noted that trace element ratios are unaffected by the corrections and normalizations that have been applied to the MI major and trace element compositions.

Volatile element compositions of MIs

Volatile concentrations in the MIs are highly variable, in the range of $0.4-2.0\,\text{wt}$ % for H_2O , $0.09-0.24\,\text{wt}$ % for S,

0.04–0.19 wt % for CI, and 0.05–0.13 wt % for F (Fig. 6). CO_2 concentrations (0.16–0.86 wt % measured; 0.19–1.83 wt % after vapor bubble correction) are amongst the highest values reported for silicate MIs, although similar or greater values have been theorized (based on gas chemistry) to be present in undegassed magmas at other alkalic volcanoes (Allard *et al.*, 1997; Gerlach *et al.*, 2002; Burton *et al.*, 2007).

H₂O and CO₂ abundances are not positively correlated with K₂O content, indicating that the variations in these elements cannot be explained by simple incompatible behavior during fractional crystallization (Fig. 6a and b). This provides evidence that the melts were vapor-saturated and had already partially degassed at the time of trapping, and/or that variable extents of post-entrapment diffusive loss of H⁺ has occurred. In contrast, all MIs have S and CI contents that generally correlate with K₂O abundance (Fig. 6c and d), which indicates that these volatiles behaved incompatibly during fractional crystallization and did not strongly partition into a vapor phase. At the lowest degree of differentiation, MIs from Hut Point, Terror, and Bird have slightly different concentrations of S and CI (Fig. 6c and d). There is no correlation between melt H₂O content and trace element enrichment (e.g. Hartley et al., 2015).

DISCUSSION

H₂O and CO₂ variations

A central goal of this study is to determine the behavior of H₂O and CO₂ in Ross Island magmas, which can be used to investigate magma storage, ascent, and differentiation. A first-order control on volatile behavior is degassing, an inevitable consequence of magma ascent owing to the strong dependence of volatile solubility on pressure (Kadik et al., 1972). Equilibrium degassing is commonly assumed for most mafic magmas because relatively high diffusivities of volatiles (owing to high temperatures) promote vapor-melt equilibrium during degassing (Sparks et al., 1994). During degassing, differences in the relative solubility of each volatile species result in fractionation, strongly affecting the CO₂/H₂O ratio of the melt and vapor phases (Dixon, 1997). Degassing models predict that an ascending magma will show a steep decline in the CO₂/H₂O ratio, owing to the low solubility of CO₂, until shallow depths where more significant H₂O degassing begins (Newman & Lowenstern, 2002; Papale et al., 2006). These models are supported by the experiments of Lesne et al. (2011) and the volatile concentrations of MIs formed in some magmatic systems (e.g. Roggensack et al., 1997; Liu et al., 2006).

The H₂O and CO₂ concentrations of MIs from Hut Point, Terror and Bird are inconsistent with modeled equilibrium degassing paths (Fig. 7). The inconsistency exists within single samples and at the volcano scale. The trend of H₂O depletion (or CO₂ enrichment), relative to equilibrium degassing paths, has been recognized in many MI suites (e.g. Spilliaert *et al.*, 2006; Johnson

et al., 2008; Vigouroux et al., 2008; Collins et al., 2009; Roberge et al., 2009; Blundy et al., 2010; Witham, 2011; Oppenheimer et al., 2011). In the following sections, several mechanisms are explored that can explain the trend, including diffusive loss of H⁺ from MIs (Roedder, 1979), disequilibrium degassing (Mangan & Sisson, 2000; Gonnermann & Manga, 2005; Pichavant et al., 2013), CO₂ fluxing (Rust et al., 2004; Spilliaert et al., 2006; Johnson et al., 2008; Vigouroux et al., 2008; Collins et al., 2009; Blundy et al., 2010), and mixing with a degassed magma (Dixon et al., 1991; Wallace & Anderson, 1998; Witham, 2011).

Volatile loss (or gain) by diffusion between MIs and carrier melt

The H₂O contents of sealed MIs can re-equilibrate with the external magma on relatively rapid timescales (Chen et al., 2011; Gaetani et al., 2012). Disequilibrium between a sealed MI and its carrier melt is caused by a change in the H₂O content of the carrier melt, most probably owing to degassing during shallow magma ascent or water loss during CO2 fluxing. The extent of MI re-equilibration is largely a function of the time and length scales and the diffusivity of H⁺ in the olivine host (Qin et al., 1992). Time, which is a function of magma ascent rate and the last depth at which the H₂O contents of a MI equilibrated, is a limiting factor, and H⁺ reequilibration is often incomplete when MIs are quenched. Otherwise MIs would not record H2O contents greater than atmospheric pressure equilibrated values (\sim 0.1 wt %). A side effect of diffusive H⁺ loss from a MI is a decrease in internal pressure that leads to increased transfer of CO2 into a vapor bubble (Bucholz et al., 2013; Moore et al., 2015; Aster et al., 2016).

Previous research has demonstrated that there is a strong link between MI radius and the extent of H₂O reequilibration (e.g. Qin et al., 1992; Chen et al., 2013; Lloyd et al., 2013). The relationship is primarily due to the control of MI size on the surface area to volume ratio. Additionally, it has been shown that near-rim MIs re-equilibrate more rapidly (Ruprecht et al., 2010). To investigate diffusive loss of H⁺, the relationship between the size and position of MIs and their H₂O content has been evaluated (Fig. 8). To eliminate the effects of variable amounts of factional crystallization that may have occurred prior to MI trapping, The H₂O contents of the MI were normalized to their Ce contents; Ce was chosen because it exhibits partitioning like that of H₂O (Michael, 1995; Danyushevsky et al., 2000). Hut Point MIs show a positive correlation between H₂O/Ce and MI radius (Fig. 8a), indicating significant diffusive loss of H⁺ from many smaller Mls. Additionally, those Mls that are closer to the edge of the host crystal tend to have reduced H₂O concentrations, consistent with diffusive loss of H⁺. The observed correlations are not especially well pronounced, but this is not surprising given that the extent to which diffusive re-equilibration occurs is a complex function of the shape, size, and position of the

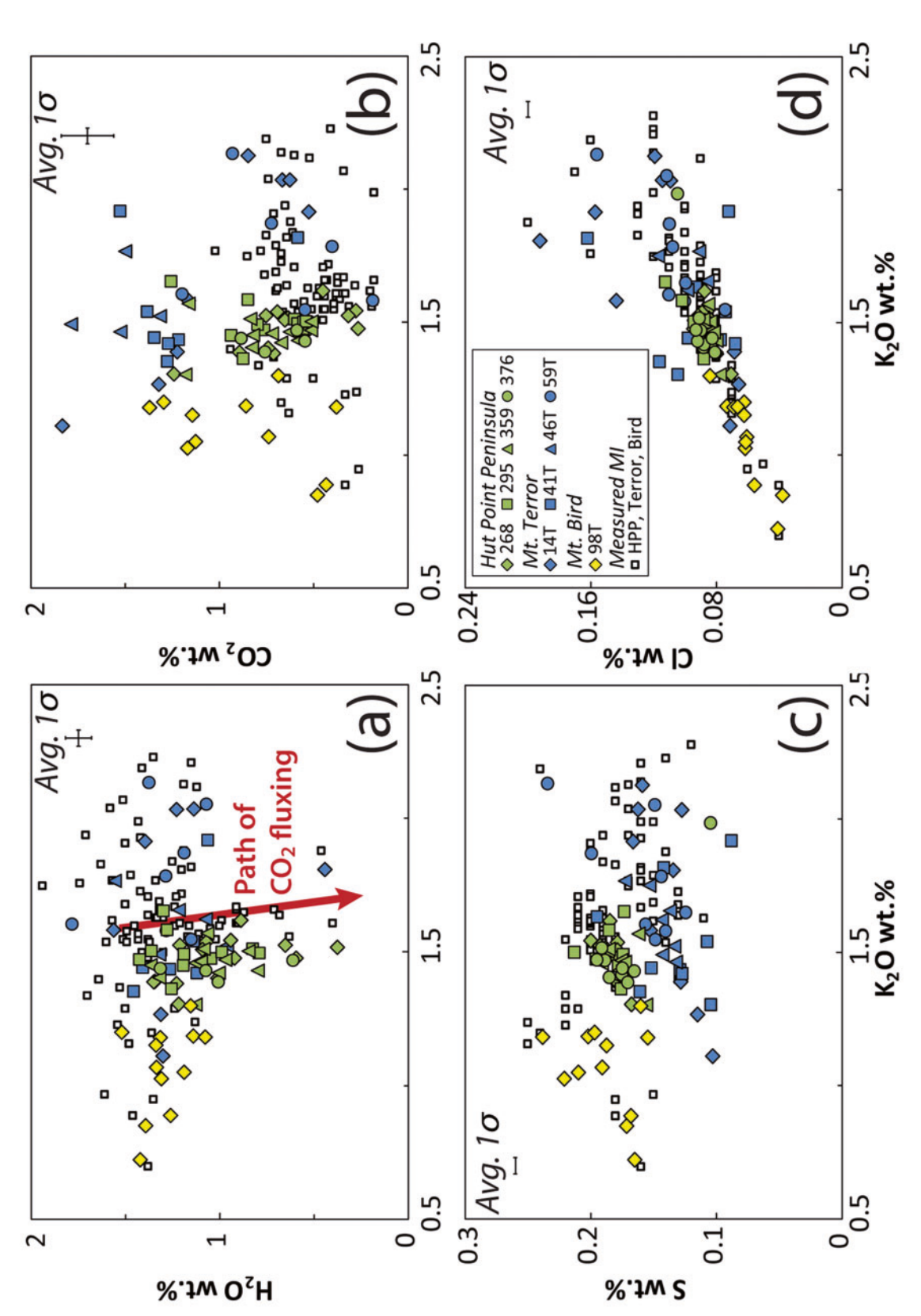


Fig. 6. Variation of K₂O and volatile contents in melt inclusions (MIs) from Ross Island. (a) The lack of a positive correlation between H₂O and K₂O indicates that simple incompatible behavior has not occurred. MI compositions are generally inconsistent with the path of CO₂ fluxing, which is calculated by assuming a loss of 1 wt % water results in a 38°C liquidus elevation (Médard & Grove, 2008) or 0·1 wt % increase in melt K₂O assuming olivine-only fractionation results (see text for details). (b) CO₂ compositions are plotted with vapor bubble addition (see text for details). The lack of correlation between CO₂ and K₂O abundances indicates that variation is not controlled by crystal fractionation. (c, d) Correlation with K₂O content suggests that variations in volatile abundances are caused by crystal fractionation.

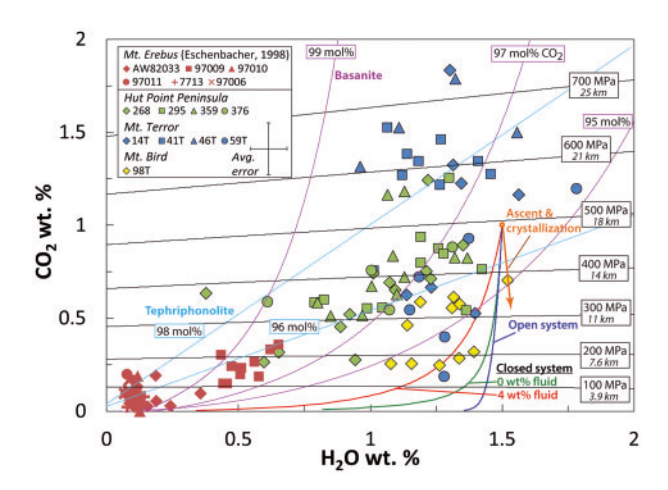


Fig. 7. H₂O vs CO₂ contents of melt inclusion (MIs) from Ross Island corrected for vapor bubble growth. Variation in MI composition is not consistent with equilibrium degassing paths (shown in orange). Erebus MI data are from Eschenbacher (1998). Isobars (black) and isopleths (purple) were calculated following the method of Iacono-Marziano *et al.* (2012), using an average of Hut Point, Terror, and Bird MI compositions. Degassing paths were modeled using VolatileCalc (Newman & Lowenstern, 2002) with the same averages, except for the path of ascent and crystallization, which is from fig. 29c of Blundy & Cashman (2008). Light blue isopleths are for more evolved compositions, which were calculated following Duan (2014), using the averaged composition of 97009 (tephriphonolite).

MI and the shape, size, and MI density of the host. In contrast to Hut Point samples, MIs from Terror and Bird lack evidence for significant diffusive loss of H⁺ (Fig. 8a and b). There are a few MIs with small radii and anomalously high values of H₂O/Ce (>150), which may have taken up H⁺ by diffusion (Koleszar *et al.*, 2009; Hartley *et al.*, 2015). It is unlikely that much of the diffusive loss of H⁺ occurred post-eruptively (i.e. Lloyd *et al.*, 2013). All the samples are expected to have quenched rapidly. Additionally, the samples that show the most pronounced effects (Hut Point samples) are hyaloclastites, which are likely to have cooled more rapidly than the samples of ash from Terror and Bird.

MI compositions converge on an H_2O/Ce ratio of ~ 130 (Fig. 8a), which is considered to be the original ratio prior to diffusive water loss. This value is considerably lower than the H_2O/Ce ratio of 200 that is associated with depleted MORB mantle (DMM) sources, indicating the involvement of a low H_2O/Ce , enriched component in the source (Dixon *et al.*, 2002). Further evidence for an enriched component in the source comes from isotopic and trace element studies that indicate mixing between HIMU and DMM sources at Ross Island (Sun & Hanson, 1975; Kyle *et al.*, 1992; Sims *et al.*, 2008).

Disequilibrium degassing

The rate at which individual volatile components move from melt to growing vapor bubbles during exsolution is controlled by the diffusivity of each component. Volatiles with low diffusivities, such as CO₂ (Watson, 1994), transfer from the melt to the vapor phase more

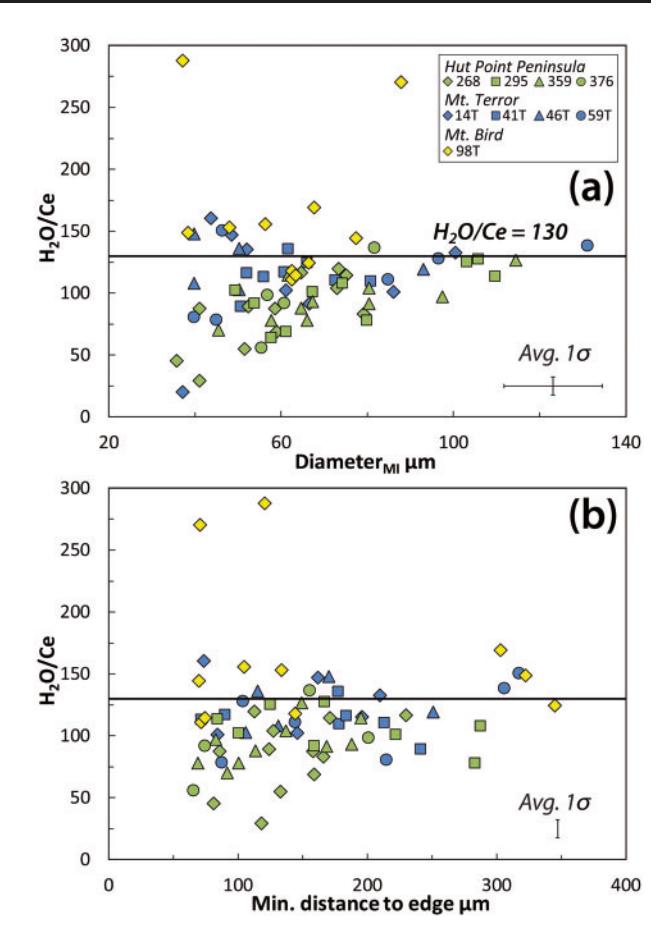


Fig. 8. Comparison of H₂O/Ce with melt inclusion (MI) size and position for Ross Island samples; H₂O/Ce converges on a value of $\sim\!130$ at increasing values of MI diameter and minimum distance to edge of the host crystal. In Hut Point samples, diffusive loss of H $^+$ is indicated by the overall tendency for low values of H₂O/Ce to be in smaller inclusions and those closer to an edge of the host. (a) The reported diameter is the average of the long and short axes of the intersected MI. (b) The minimum distance to edge is measured from the center of the MI to the nearest crystal face.

slowly and can become significantly super-saturated in a melt during disequilibrium degassing. This process is typically associated with mid-ocean ridge basalts (e.g. Sarda & Graham, 1990) and felsic magmas (e.g. Mangan & Sisson, 2000; Gonnermann & Manga, 2005). The experiments of Pichavant *et al.* (2013) show that other mafic magmas can also be susceptible. Experiments demonstrate that this process becomes important when vesicle number densities are low because the volatile exsolution is limited by the associated time and length scales of diffusion (Pichavant *et al.*, 2013).

One way to evaluate the likelihood of disequilibrium degassing is to consider bubble nucleation during exsolution. From experimental studies, there is no consensus about whether high alkali contents promote (e.g. Gardner, 2012) or inhibit (e.g. Bagdassarov *et al.*, 2000) bubble nucleation. Vapor bubbles occupy a variable percentage (1–22%) of the MI volume in the Ross Island samples (Supplementary Data Table EA3.4). The

significant variation, even in a single sample, of vapor bubble volume per cent indicates that a separate vapor phase was probably co-entrapped with some Mls, perhaps causing a defect at the crystal-liquid interface and resulting in MI formation (e.g. Roedder, 1979). If some of the vapor bubbles were in fact co-entrapped, it would follow that vesicle number densities were high in the carrying magma, which favors equilibrium degassing behavior. It is also important to note that the experiments of Pichavant et al. (2013) were largely crystal-free, and bubble nucleation was therefore homogeneous. A more likely case for a crystal-bearing natural system, such as the Ross Island one, is heterogeneous bubble nucleation. Heterogeneous bubble nucleation requires a lower degree of volatile super-saturation (Mangan & Sisson, 2000), and it follows that disequilibrium conditions are favored during homogeneous nucleation. Although the possibility of disequilibrium degassing cannot be completely ruled out, we note that high inferred vesicle number densities and the likelihood of heterogeneous bubble nucleation indicate that this process may not have been significant at Ross Island.

CO₂ fluxing

CO2 fluxing (also called CO2 flushing) is the most commonly invoked mechanism to explain non-equilibriumdegassing behavior (e.g. Rust et al., 2004; Spilliaert et al., 2006; Johnson et al., 2008; Vigouroux et al., 2008; Collins et al., 2009; Blundy et al., 2010). CO2 fluxing occurs when a CO2-rich vapor emanating from depth percolates through magma. Exchange of H₂O and CO₂ between the vapor and melt results from chemical disequilibrium; dissolution of CO2 is less pronounced owing to its slow diffusion rate (Yoshimura & Nakamura, 2010). H₂O diffuses about an order of magnitude faster (Watson, 1994), and significant transfer of water to the vapor can occur (Yoshimura & Nakamura, 2010). The fluxing vapor can be generated by conduit degassing (e.g. Rust et al., 2004), degassing of deep melts (e.g. Spilliaert et al., 2006; Johnson et al., 2008; Blundy et al., 2010), or assimilation of crustal carbonates (e.g. Marianelli et al., 2005).

One way to test for CO₂ fluxing is to consider the expected effects. Modeled vapor isopleths predict the range of H₂O and CO₂ contents of a melt in equilibrium with a vapor of fixed composition. Therefore, the divergence of MI compositions from an equilibrium degassing path towards a vapor isopleth is expected if CO2 fluxing has occurred. Vapor isopleths in Fig. 7 demonstrate that fluxing of a CO₂-rich vapor (97-99 mol % CO₂) could cause the observed H₂O and CO₂ trends in the Terror and Bird Mls. However, there are several lines of evidence that are inconsistent with a CO₂ fluxing interpretation. First, magma dehydration during CO₂ fluxing results in solidus elevation, which induces crystallization (Johnson et al., 2008). A decrease in melt H₂O content of 1 wt % results in a 38 ± 5 °C liquidus elevation of an olivine-saturated melt (Médard & Grove, 2008). This degassing-induced undercooling has been modeled by simulating the isobaric cooling of a melt (with the composition of primitive MI, 59T-32) using Petrolog3 (Danyushevsky & Plechov, 2011) and applying the olivine-melt model of Danyushevsky (2001). The result for 1 wt % of water loss was ~3.7 wt % of olivine crystallization and a corresponding increase of melt K₂O content by 0.1 wt %. Thus, a negative correlation, albeit minor, would be expected between H₂O and K₂O contents if CO₂ fluxing had occurred. A negative correlation is not observed between melt H₂O content and extent of fractionation in most samples (Fig. 6a). Hut Point MI compositions show a similar trend. However, K2O abundance increases with decreasing CO₂ content (Fig. 6b), which is not expected for CO2 fluxing, and diffusive water loss has been identified in these Mls. Second, CO2 fluxing is often considered to occur isobarically (e.g. Spilliaert et al., 2006; Collins et al., 2009), which is because the fluxing vapor must ascend rapidly relative to the melt to avoid dilution by water that partitions from the melt into the CO₂-rich vapor. If there is a constant supply of CO2-rich vapor ascending rapidly relative to the magma, the dilution of the vapor phase (to a lower mole fraction of CO₂) will be less important. Isobaric CO₂ fluxing results in declining magmatic water concentration along a vapor saturation isobar and isobaric crystallization. The Ross Island MI data are not consistent with these processes. The composition of one sample (41T) has some attributes that can be explained by isobaric dehydration (Fig. 7), but the data for this sample are inconsistent with isobaric fractionation (Fig. 6a).

Despite the lack of evidence supporting CO₂ fluxing as a primary control on melt H2O and CO2 at Terror or Bird, it is still likely that this process has occurred to some extent. We have shown evidence of high magmatic CO₂ concentrations and early CO₂ saturation, and Eschenbacher (1998) demonstrated that the modern CO₂ emissions from Erebus volcano are high relative to predictions based on magma supply rate and the CO₂ contents of Hut Point Mls. It is likely that a deeply derived CO2-rich vapor could have interacted chemically with hydrous magmas during ascent (Yoshimura & Nakamura, 2010). One way to explain the apparent lack of evidence for CO₂ fluxing is that melt dehydration may have been minor. Variable vapor bubble volume per cent provides evidence that exsolved vapor is likely to have been abundant at the time of MI entrapment. If the separate vapor phase contained H₂O, it would buffer magmatic volatile contents during fluxing, diminishing the dehydration effects (Yoshimura & Nakamura, 2010). Another possible explanation is that CO2 fluxing may not have been important until after MI entrapment, in which case it would have contributed to diffusive H⁺ loss, particularly in small Mls.

Drain-back mixing

It has been shown that mixing of undegassed and degassed magma (drained back from shallow depths)

can result in a non-equilibrium-degassing trend (Witham, 2011), which is a process that occurs at Kilauea volcano, Hawaii (Dixon et al., 1991; Wallace & Anderson, 1998). Shallow magmas that have cooled and degassed H₂O become negatively buoyant and sink. The descending magma mixes and re-equilibrates with the surrounding magma as it descends. H₂O diffuses more rapidly than CO2 in the melt, which nudges the melt compositions away from the equilibrium degassing trends. At Ross Island, drain-back mixing is unlikely. MIs have consistently high concentrations of S (Fig. 6c), which is inconsistent with mixing with a shallowly degassed magma (Dixon et al., 1991). Additionally, degassing of H₂O does not occur until depths that are much shallower than MI entrapment depths (Fig. 7). Thus, this process would require magmas to descend for tens of kilometers (Fig. 7).

Mixing of diverse magmas

Mixing of magma batches containing MI-bearing olivine could significantly affect the distribution of the H₂O and CO₂ contents of the MIs within a single eruptive unit. MIs that formed in different magmas and experienced different pre-eruptive histories would not necessarily follow a coherent degassing path. Variability in melt H₂O and CO₂ contents could arise in several different scenarios. Melts parental to the MI could travel along slightly different *P-T-t* paths, undergoing different crystallization histories. MIs may have resided at different depths in the crust for different lengths of time, CO₂ fluxing may have affected some melts but not others, and primary melts could be formed from slightly different extents of partial melting. These processes all have the potential to influence the behavior of H₂O and CO₂.

MI compositions from this study, especially those from Terror and Bird, do not form tight arrays on major, trace, or volatile element plots (Figs 3-6). The K₂O/TiO₂ ratio, which is not affected by PEC or diffusive exchange of Fe-Mg or H+, is useful for assessing the mixing of different olivine and MI populations (Fig. 9). Unlike in MI suites from Iceland (e.g. Maclennan, 2008), MI compositional heterogeneity in the Ross Island samples does not decrease with magmatic differentiation, suggesting that the variations are not caused primarily by concurrent mixing and crystallization. Rather, most MI entrapment appears to have occurred prior to mixing. Bird MIs appear to form a mixing array on some plots (e.g. Figs 4c, d and 9), which would be expected if mixing occurred during or before MI entrapment. However, as discussed above, the trend is mostly due to the influence of two MIs (98 T-4 and 98 T-12) with anomalously low Ce contents (e.g. Fig. 8).

The chemical variability observed in Ross Island MIs is common to MI suites from elsewhere (Kent, 2008). For Ross Island, the heterogeneity is at least partly inherited from variability in the parental melts, as indicated by the wide spread in Dy/Yb of the MIs, which cannot be due to fractionation alone (Fig. 5). Dy/Yb is

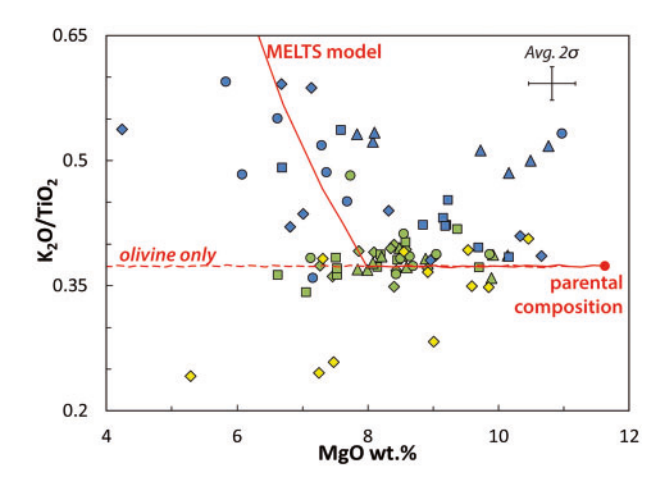


Fig. 9. K₂O/TiO₂ ratios vs MgO content for melt inclusions (MIs) from Ross Island. The trends indicate that MIs formed from melts of different composition. Lines show results of MELTS models, which are the same as in Fig. 4.

particularly sensitive to the presence of garnet in the residue during mantle melting. Variation could be related to the modal abundance of garnet in the source or to the extent of partial melting.

There are two possible scenarios to describe how MIs that formed in different melts could have later become incorporated into the same magma. First, some of the MI-bearing olivines could be cumulates that were re-entrained during the ascent of a later magma batch. This phenomenon has been suggested to occur at Kilauea volcano (Fodor & Moore, 1994). Support for reentrainment of cumulates at Terror comes from the abundance of olivine-rich xenoliths, which are probably cumulates, in its eruptive products (Wright & Kyle, 1990b). Second, Terror magmas could have formed by batch assembly, meaning that MIs formed in different batches of magma that were later mixed and then erupted together as a single unit. Such a process is likely to happen beneath Ross Island, where small volumes of melt are produced during low degrees of partial melting (3-7%; Sun & Hanson, 1975).

Regardless of the source of the chemical variation, the implication of this finding is that complex histories, potentially involving the overprinting of several different processes that influence the behavior of H_2O and CO_2 , can explain the lack of any evidence found for a single primary control on MI H_2O and CO_2 . For Hut Point, the non-equilibrium degassing behavior can be attributed primarily to diffusive loss of H^+ .

Open-system processes

Additional evidence for open-system processes in samples from Terror and Bird comes from the observation that bulk-rock compositions are more evolved than those of the MIs (except 59 T), and matrix glass compositions are highly variable, although they typically lie within the bulk-rock compositional arrays (Fig. 3). All samples contain high-Fo olivine (Fo₈₈₋₉₁), which occurs with plagioclase, alkali feldspar and kaesutite. Most

kaersutite crystals are reversely zoned, with 30–270 µm thick rims. Kaersutite cores typically have rounded edges (Supplementary Data Fig. EA5.1), indicating that dissolution occurred at some stage followed by new growth episodes. As noted above, MI compositions for the most part do not lie along mixing arrays, an aspect that is interpreted to indicate that compositions have been controlled by processes occurring postentrapment. It is suggested that the parental magma for the MIs either mixed with a more evolved, kaersutite-bearing magma or interacted with a crystal-rich mush.

Further complicating the pre-eruptive histories of the Terror and Bird samples is the occurrence of xenocrystic orthopyroxene, which is not a crystallizing phase in basanites, and high-Fo, low-Ca olivine. Both phases were likely to have derived from the mantle. If this is the case, the xenocrysts must have survived transportation through >25 km of crust (Finotello *et al.*, 2011), implying a relatively short period of crustal residence.

Magmatic plumbing system

Magma storage

A standard method to investigate crystallization depths (and infer storage depths) using MI compositions is to model vapor saturation pressures (e.g. Metrich & Clocchiatti, 1989), which requires the assumptions that the melts were vapor saturated at the time of trapping and that the internal pressure (or pressure of last equilibration) of the MI was maintained throughout ascent and eruption. For the Ross Island MIs, the first assumption is reasonable. CO2 is the least soluble of the measured volatile species and does not behave as an incompatible element in melt evolution diagrams (e.g. Fig. 6b), which is robust evidence that the melt parental to the MI was vapor saturated during MI entrapment. The second assumption poses a difficulty. The effects of decompression of the external melt on the internal pressure of a melt inclusion have been shown to be generally minor (Tait, 1992) and the CO2 contents have already been corrected to account for CO2 loss to bubbles inside the MIs during cooling and PEC of olivine. However, diffusive loss of H⁺ after trapping also causes an internal drop in pressure (Bucholz et al., 2013), and this has not been accounted for in the present study. MIs from Hut Point, and possibly those from Terror and Bird to some extent, have undergone diffusive loss of H⁺. This phenomenon is explored in this section. It is stressed that pressure estimates should be viewed as minimum values. It is also noted that in using the eruptive products of monogenetic vents to make inferences about the plumbing system of each volcano, there is potential for bias in the record of information obtained.

To determine vapor saturation pressures, the model proposed by lacono-Marziano *et al.* (2012) has been used because it is specifically calibrated for mafic compositions, including alkali basalts. Mls from Hut Point, Terror, and Bird record vapor saturation pressures between 160 and >560 MPa, which correspond to depths

of 6 to >19 km. This upper limit approaches the Moho depth for the region (19–27 km; Finotello *et al.*, 2011).

All four of the Hut Point samples belong to a single unit of hyaloclastite with remarkably minor chemical variation and only tenuous evidence of a single erosive break (Kyle, 1981a), which could indicate that the magmas were sourced from a stable, well-mixed reservoir. If the magmas parental to the Hut Point MIs were stored in a hypothetical reservoir, a locus of melt inclusion vapor saturation pressures would be expected. However, we have already argued that these MIs have undergone a variable degree of diffusive loss of H⁺, which lowered the internal pressure of the MIs. The initial H₂O contents of the MIs can be inferred by assuming an H₂O/Ce ratio of 130, which the MI compositions appear to converge upon (Fig. 8). Using the difference between calculated H_2O and observed H_2O contents (termed ΔH_2O), the extent of diffusive loss of H⁺ can be approximated, assuming minimal water was lost (or gained) from the initial melts by different processes. Interestingly, ΔH_2O varies approximately linearly with vapor saturation pressure for MIs from Hut Point. This nearly linear drop in internal pressure with diffusive loss of H+ has been observed elsewhere (Mironov et al., 2015). It has been suggested that the internal pressure of MIs decreases during diffusive loss of H⁺, resulting in the additional transfer of CO₂ into each vapor bubble (Bucholz et al., 2013). CO2 in the bubble has already been allowed for by adding CO₂ back into the MI compositions, but this approach only accounts for the effects of cooling and crystallization of olivine. Thus, the pressure decrease that correlates with a decline in H₂O content must be due to additional vapor bubble growth caused by diffusive loss of H⁺. The correlation implies that the Hut Point melt inclusions formed at a similar depth. If the trend is extrapolated to $\Delta H_2O = 0$, a pressure of about 500 MPa, corresponding to a depth of \sim 18 km, can be inferred for MI entrapment and magma storage.

Terror and Bird magmas are unlikely to have resided in large, stable magma reservoirs. The compositions of MIs from these volcanoes are inconsistent with isobaric entrapment, which would be expected if the MIs reflected crystallization in a magma chamber. Additionally, there is no systematic relationship between ΔH_2O and entrapment pressure (Fig. 10). Furthermore, eruptive products from these volcanoes are commonly primitive in composition and contain abundant mantle xenoliths (Kyle, 1990b; Wright & Kyle, 1990a, 1990b), despite the fact that the magmas ascended through more than 20 km of crust (Finotello et al., 2011). Interestingly, mantle xenoliths are abundant at Hut Point in surface samples, but they are absent from the unit studied in the DVDP core. It is possible that the DVDP samples track an earlier stage in the evolution of the volcanic plumbing system during which a more established reservoir existed. Later eruptive products may have bypassed the reservoir or it may have become inactive.

Evidence has been presented to show that Terror and Bird magmas mixed with a more evolved magma,

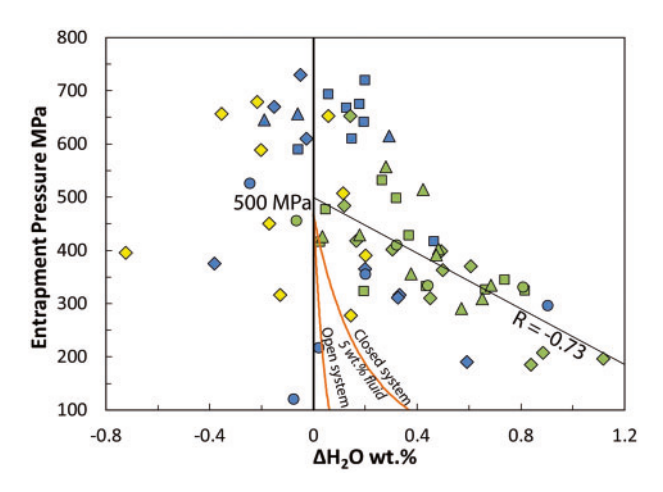


Fig. 10. Relationship between H_2O loss and modeled entrapment pressure for Ross Island melt inclusions (MIs), showing that MIs in which diffusive loss of H^+ has occurred have entrapment pressures that are low relative to MIs that have not lost H^+ . Only the samples with trace element data that have been corrected for vapor bubble formation are shown. ΔH_2O is the difference between calculated H_2O concentration (assuming H_2O /Ce of 130) and observed H_2O concentration. Open- and closed-system degassing paths are the same as in Fig. 7. The linear regression is for all Hut Point samples that have a positive value of ΔH_2O .

which is likely to have been stored at shallow depths. The presence of xenoliths in two samples (59T and 98T) and the lack of dissolution textures in orthopyroxene in all samples are evidence for short crustal residence times. Thus, the ascending mafic magmas would have had to interact only briefly with the more evolved magma prior to eruption. Volumetrically minor amounts of evolved basanite to phonolite are found at all three volcanoes (Kyle, 1990b; Wright & Kyle, 1990a, 1990b), indicating the potential existence of relatively small reservoirs where magma can stall and evolve in the cool upper crust.

Magma ascent

The ascent rate of Hut Point magmas can be quantified by considering the extent of diffusive re-equilibration of H⁺ in MIs because this process is limited by the rate of diffusion of H⁺ and occurs during magma ascent and post-eruptive slow cooling (Lloyd et al., 2013). H⁺ loss owing to slow cooling is assumed to be negligible because the Hut Point samples are hyaloclastites. The H⁺ diffusion model of Chen et al. (2013), which is based on the solution of Qin et al. (1992), has been applied. Chen et al. (2013) invoked the coupled proton and metal vacancy diffusion mechanism (Demouchy & Mackwell, 2006), the slower of the two H⁺ diffusion mechanisms in olivine. The metal vacancy diffusion mechanism is preferred here because it is supported by recent MI dehydration experiments (Chen et al., 2011; Gaetani et al., 2012; Bucholz et al., 2013), and under reducing conditions, the faster of the mechanisms (proton-polaron; Mackwell & Kohlstedt, 1990) is likely to be less important. The Chen et al. (2013) model incorporates variable

boundary conditions for temperature and external melt H₂O concentration. For initial temperature, we used our estimates of entrapment temperature, and final temperature was set to the quench temperature (using the methods outlined above). For external water, three ascent scenarios have been modeled, using degassing calculated with VolatileCalc (Newman & Lowenstern, 2002), and these are shown in Fig. 7. It is assumed that all MIs were entrapped at 500 MPa or 18 km depth (Fig. 10), and that all MIs were carried in magmas that followed the same degassing path. The initial H₂O concentrations were calculated using an H₂O/Ce ratio of 130, and an average value of Ce, which yielded 1.5 wt 3% H₂O. It should be noted that this is a simplification and a limitation of the model. However, it is inferred that magma compositions may have been homogenized in a reservoir beneath Hut Point, resetting MI H₂O contents to a single value.

Model results vary significantly between the three degassing scenarios, with the largest offset occurring between results for an open-system degassing model and the two closed-system degassing cases. Ascent rates vary over about three orders of magnitude $(\sim 5 \times 10^{-4} \text{ to } 4 \times 10^{-1} \text{ m s}^{-1}; \text{ Fig. 11a}), \text{ and the time for }$ magma ascent to occur ranges from ~1 day to 1 year (Fig. 11b). These estimates assume constant ascent rates from mid- to lower crustal depths (~18 km) to the surface. A more likely scenario is that magma ascends at an increasing rate as volatiles exsolve and add buoyancy to the melt, and at shallower depths, diffusive loss of H⁺ becomes more important as the gradient between the MI H₂O contents and the external melt increases as water begins to degas. The most likely scenario is that magma initially ascends more slowly than our calculated rates, and as magmas ascend the velocity increases to rates greater than our predictions. Additionally, CO₂ fluxing may have affected the melt in the host magma after MI entrapment. A larger H⁺ concentration gradient would develop at greater depth, requiring faster magma ascent. Thus, ascent rates should be taken as minimum values.

Few studies have constrained magma ascent rates from mid- to lower-crustal depths (e.g. Armienti et al., 2012; Ruprecht & Plank, 2013). Despite the significant variability, the model results presented here put important constraints on the system. The minimum ascent rates of the model overlap with those obtained by Ruprecht & Plank (2013), which are mantle-to-surface ascent rates based on Fe-Mg interdiffusion in olivine. The results modeled here require that magmas ascended from depths of 18 km to the surface in less than a year. The high end of these modeled ascent rates overlaps with estimates for ascent from mid- to uppercrustal reservoirs (Lloyd et al., 2013, 2014). Also within this range are 2-10 m s⁻¹ ascent rates, based on xenolith settling velocities, obtained for alkalic magma by Rutherford & Gardner (1999), based on xenolith settling velocities. Our results underscore the importance of understanding the degassing path of the melt in the

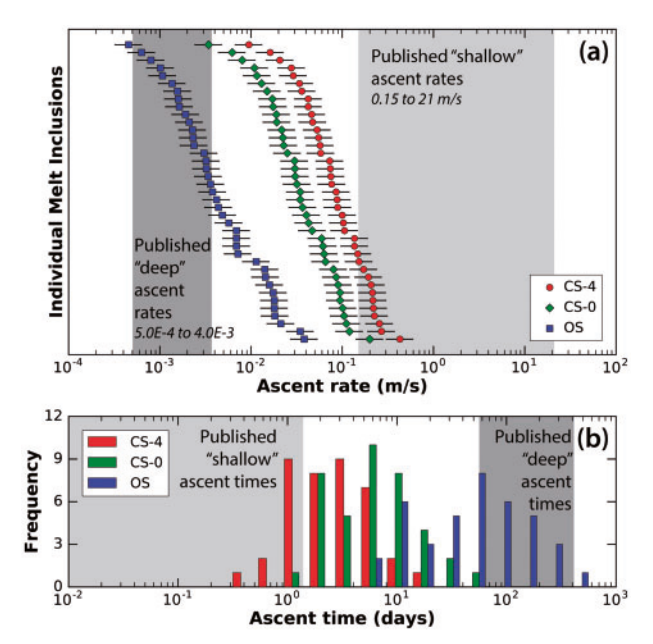


Fig. 11. Magma ascent rates and ascent times for three degassing scenarios (shown in Fig. 7) for Ross Island melt inclusions (MIs) and comparisons with other estimates. CS-4 is closed system, 4 wt % exsolved fluid. CS-0 is closed-system, 0 wt % exsolved fluid. OS is open system. (a) Results of diffusion modeling for individual Mls. Both cases of closed-system degassing yield similar results. Error bars reflect the uncertainty in temperature. Published 'deep' ascent rates give the ascent rate through the entire crust (Ruprecht & Plank, 2013). Published 'shallow' ascent rates are estimates for ascent from a crustal reservoir to the surface (Rutherford & Gardner, 1999; Lloyd et al., 2013, 2014). (b) Histogram of magma ascent time from an 18 km deep reservoir. All but one of the estimates is consistent with magma ascending from a deep crustal reservoir in less than 1 year. Published 'deep' and 'shallow' ascent times are based on ascent rates referenced in (a) applied to ascent from 18 km.

host magma when modeling MI dehydration. A good approach to this problem is to examine large MIs, which are likely have lost less H⁺, and to obtain an empirical degassing path. For Ross Island, that was not possible because the studied MIs were entrapped at great depth and most MIs lost significant H⁺ during ascent.

Ascent rates calculated for Hut Point should be taken as minimum values for Terror and Bird samples, which contain MIs with less conspicuous evidence of diffusive loss of H⁺. Greater abundance of microlites in the Hut Point samples (>80%) relative to Terror (<10-35%) and Bird (30-70%) samples corroborates this interpretation (Supplementary Data Fig. EA5.4). Because Hut Point samples are rapidly quenched marine hyaloclastites, microlite crystallization is likely to be pre-eruption in origin. Differences in the characteristics of the volcanic systems at Hut Point, Terror, and Bird could explain the differing ascent rates. Each edifice differs in size. Terror and Bird have large volumes (1700 and 470 km³, respectively) relative to Hut Point (100 km³). The load imposed by an edifice has been shown to influence the development of ascending dikes (Karlstrom et al., 2009). Perhaps Hut Point has a less developed network of dikes, resulting in slower magma ascent, owing to its relatively small size. An additional factor could be the location of the volcanic centers. Most of the recent extension in the Terror Rift has occurred to the north of Ross Island (Hall *et al.*, 2007). Terror and Bird are closer to the influence of this extension, which could promote dike formation and rapid magma transport through areas of weaker crust (Gudmundsson, 2006).

Comparison with Erebus

In this section, the H₂O and CO₂ contents of olivinehosted MIs from Erebus previously studied by Eschenbacher (1998) and Oppenheimer et al. (2011) are re-examined and comparisons are made with results from the present study. The Erebus samples are from localities SE of the summit and have compositions and mineral assemblages consistent with the eruptive products of the volcano, which has led to the suggestion that they belong to the same differentiation series (Eschenbacher, 1998). Erebus whole-rock compositions define a single liquid line of descent, like those of the surrounding volcanoes (Fig. 3), that ranges from evolved basanite to phonolite. Using a least-squares mass-balance approach, Kyle et al. (1992) suggested that Erebus magmas have a similar parent to magmas erupted at Hut Point, However, differences in the mineralogy of the Erebus and Hut Point samples (importantly, the lack of kaersutite in Erebus rocks) indicate that the Erebus magmas undergo hotter, drier differentiation (Kyle et al., 1992), which is supported by a recent phase equilibria study (lacovino et al., 2016).

H_2O and CO_2 concentrations of Erebus melt inclusions

Relative to other Ross Island volcanoes, Erebus samples have low concentrations of H_2O and CO_2 ($\sim\!0.1\,\text{wt}$ % H_2O and $\sim\!0-0.2\,\text{wt}$ % CO_2 , except 97009, which has slightly elevated values of 0.5–0.7 wt % and 0.1–0.4 wt %, respectively; Fig. 7), compared with the surrounding volcanoes (0.4–2.0 wt % H_2O and 0.2–1.8 wt % CO_2 ; Fig. 7). The H_2O contents of Erebus MIs cannot be reconciled with a standard model of melt evolution (path of ascent and crystallization in Fig. 7).

Erebus MIs were entrapped at low pressure (most <150 MPa). Low H₂O (\sim 0.1 wt %) and CO₂ (<0.2 wt %) concentrations in most MIs are inconsistent with equilibrium degassing of H₂O in a shallow magma chamber (Fig. 7). High emissions of CO₂ from Erebus led Eschenbacher (1998) to suggest a persistent flux of deeply derived CO2 through the magmatic system. CO2 fluxing could potentially result in H2O and CO2 trends of Erebus MIs (Fig. 7), which was previously suggested by Oppenheimer et al. (2011). To explain the low-H₂O, elevated-CO2 MIs, the fluxing vapor would have to be extremely CO₂-rich (>98 mol % CO₂) and vapor-melt equilibrium would need to follow tephriphonolite isopleths (Fig. 7). These isopleths differ in shape from those predicted for the same composition magma by other models (e.g. Papale et al., 2006), which are similar in

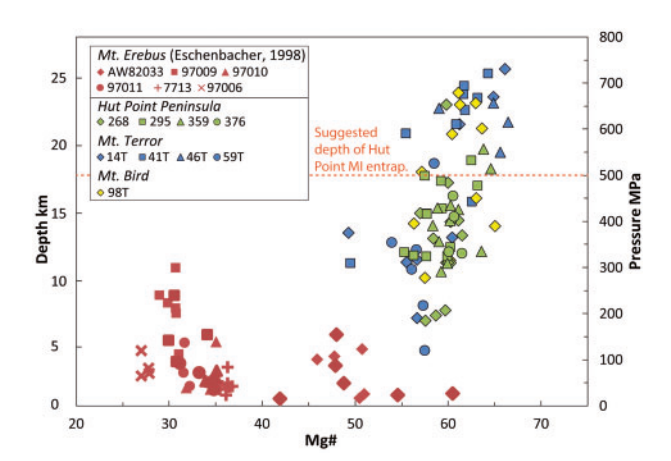


Fig. 12. Pressures (and depths) of formation vs Mg# [molar Mg/(Mg + Fe^{2+})] for Ross Island melt inclusions (MIs). Erebus data give consistently lower pressures than data for other volcanoes. All MIs have been corrected for PEC and vapor bubble growth (in the cases where a bubble was present). MIs from Erebus lack vapor bubbles (Eschenbacher, 1998). The dashed orange line indicates the inferred depth of formation of Hut Point MIs (see Fig. 10).

shape to the basanite isopleths (Fig. 7). Diffusive loss of H^+ is a possible explanation for the low H_2O contents of Erebus MIs. However, the MIs lack vapor bubbles, which would require resorption of bubbles formed during diffusive loss of H^+ during heating of the MIs after entrapment. Another possibility is that Erebus magmas are inherently drier than those of the surrounding volcanoes.

Erebus plumbing system

MI entrapment pressures provide evidence for extensive shallow crystallization at Erebus (Fig. 12), perhaps indicating the existence of a shallow storage region. MI compositions range from basanite to phonolite, and most (83%) have been entrapped at pressures of <150 MPa, corresponding to depths of <6 km (Fig. 12). The presence of a shallow reservoir is supported by radioactive equilibrium between (210Pb/226Ra) and (²²⁷Ac/²³¹Pa), which indicates long (>100 years) residence times for the Erebus phonolitic magmas (Sims et al., 2013). Shallow storage was also proposed by Oppenheimer et al. (2011), who, however, suggested that most differentiation and dehydration occurs in a deep reservoir (>800 MPa). The wide range of chemical compositions observed at shallow depth indicates that either differentiation is shallow or that some melts bypass a hypothetical deep region of differentiation. The later scenario requires that for differentiated melts, the deep crystallization is not recorded in Mls.

CONCLUSIONS

 $\rm H_2O$ (0.4–2.0 wt %) and $\rm CO_2$ (0.2–1.8 wt %) variations in MIs from Hut Point, Terror, and Bird are inconsistent with modeled equilibrium degassing paths. MIs from Hut Point underwent post-entrapment diffusive reequilibration of $\rm H^+$. Diffusion model estimates of magma ascent are interpreted to indicate that Hut Point

magmas ascended from depths of $\sim\!18\,\mbox{km}$ in less than a year, but the results strongly depend on the degassing path of the melt in the host magma. Mls from Terror and Bird lack a strong indication of diffusive loss of H^+ , indicating that the magmas ascended more rapidly. The inferred differences in ascent rate are reflected in the abundance of microlites in the samples. The H_2O and CO_2 contents in Terror and Bird Mls require more complex pre-eruptive histories, which probably have been influenced by magma mixing. For all samples, there is no direct evidence of CO_2 fluxing.

Mls were entrapped over a wide range of pressures (160 to >560 MPa). Adjusting for the effects of diffusive loss of H⁺ and vapor bubble growth, the Hut Point Mls are likely to have been entrapped at \sim 18 km depth. The Terror and Bird Ml compositions reflect polybaric entrapment and contain xenocrystic material. The most likely scenario for these volcanoes is that magmas ascend relatively rapidly through a network of sills and dikes.

MIs from Erebus (Eschenbacher, 1998) have low H_2O and CO_2 concentrations (most ~ 0.1 wt % and $\sim 0-0.2$ wt %, respectively). Calculated MI vapor saturation pressures indicate significant shallow (< 6 km) crystallization at Erebus. This shallow differentiation is not observed at the surrounding volcanoes.

MI studies that assess the H_2O and CO_2 contents of MIs must consider diffusive loss of H^+ . We have demonstrated the importance of evaluating MI morphology and textural indications of ascent rate in host tephras. We also underscore the importance of careful interpretation of MI data and working with a sufficiently large dataset, because the compositions of individual MIs, even within the products of a single eruption, sometimes are influenced by different pre-eruptive histories.

ACKNOWLEDGEMENTS

We would like to offer our great appreciation to Jacob Lowenstern and two anonymous journal reviewers for thoughtful comments that helped improve this paper. D.J.R. would like to thank William McIntosh and Terry Plank for discussions that helped advance the paper. We would like to express our appreciation to everyone who helped with the data acquisition, including John Donovan, Nelia Dunbar, Lynn Heizler, Adam Kent, and Richard Bradshaw. The DVDP samples were provided by the US Polar Rock Repository (PRR) at Ohio State University. The PRR is supported by the National Science Foundation Office of Polar Programs.

FUNDING

This work was supported by NSF grant ANT1141534.

SUPPLEMENTARY DATA

Supplementary data for this paper are available at *Journal of Petrology* online.

REFERENCES

- Allard, P., Carbonnelle, J., Dajlevic, D., Bronec, J. L., Morel, P., Robe, M. C., Maurenas, J. M., Faivre-Pierret, R., Martin, D., Sabroux, J. C. & Zettwoog, P. (1991). Eruptive and diffuse emissions of CO₂ from Mount Etna. *Nature* **351**, 387–391.
- Allard, P., Jean-Baptiste, P., D'Alessandro, W., Parello, F., Parisi, B. & Flehoc, C. (1997). Mantle-derived helium and carbon in groundwaters and gases of Mount Etna, Italy. *Earth and Planetary Science Letters* **148**, 501–516.
- Armienti, P., Perinelli, C. & Putirka, K. D. (2012). A new model to estimate deep-level magma ascent rates, with applications to Mt Etna (Sicily, Italy). *Journal of Petrology* **54**, 795–813.
- Armstrong, R. L. (1978). K–Ar dating: Late Cenozoic McMurdo Volcanic group and dry valley glacial history, Victoria Land, Antarctica. New Zealand Journal of Geology and Geophysics 21, 685–698.
- Aster, E. M., Wallace, P. J., Moore, L. R., Watkins, J., Gazel, E. & Bodnar, R. J. (2016). Reconstructing CO₂ concentrations in basaltic melt inclusions using Raman analysis of vapor bubbles. *Journal of Volcanology and Geothermal Research* 323, 148–162.
- Bagdassarov, N., Dorfman, A. & Dingwell, D. B. (2000). Effect of alkalis, phosphorus, and water on the surface tension of haplogranite melt. *American Mineralogist* 85, 33–40.
- Behrendt, J. C. (1999). Crustal and lithospheric structure of the West Antarctic Rift System from geophysical investigations— a review. *Global and Planetary Change* **23**, 25–44.
- Blundy, J. & Cashman, K. (2008). Petrologic reconstruction of magmatic system variables and processes. In: Putirka, K. D. & Tepley, F. J., III (eds) Minerals, Inclusions and Volcanic Processes. Mineralogical Society of America and Geochemical Society, Reviews in Mineralogy and Geochemistry 69, 179–239.
- Blundy, J., Cashman, K. V., Rust, A. & Witham, F. (2010). A case for CO₂-rich arc magmas. *Earth and Planetary Science Letters* **290**, 289–301.
- Bucholz, C. E., Gaetani, G. A., Behn, M. D. & Shimizu, N. (2013). Post-entrapment modification of volatiles and oxygen fugacity in olivine-hosted melt inclusions. *Earth and Planetary Science Letters* 374, 145–155.
- Burton, M., Allard, P., Muré, F. & La Spina, A. (2007). Magmatic gas composition reveals the source depth of slug-driven Strombolian explosive activity. *Science* **317**, 227–230.
- Chen, Y., Provost, A., Schiano, P. & Cluzel, N. (2011). The rate of water loss from olivine- hosted melt inclusions. *Contributions to Mineralogy and Petrology* **162**, 625–636.
- Chen, Y., Provost, A., Schiano, P. & Cluzel, N. (2013). Magma ascent rate and initial water concentration inferred from diffusive water loss from olivine-hosted melt inclusions. Contributions to Mineralogy and Petrology 165, 525–541.
- Cole, J. W. & Ewart, A. (1968). Contributions to the volcanic geology of the Black Island, Brown Peninsula, and Cape Bird areas, McMurdo Sound, Antarctica. New Zealand Journal of Geology and Geophysics 11, 793–828.
- Collins, S. J., Pyle, D. M. & Maclennan, J. (2009). Melt inclusions track pre-eruption storage and dehydration of magmas at Etna. *Geology* **37**, 571–574.
- Cooper, A. F., Adam, L. J., Coulter, R. F., Eby, G. N. & McIntosh, W. C. (2007). Geology, geochronology and geochemistry of a basanitic volcano, White Island, Ross Sea, Antarctica. *Journal of Volcanology and Geothermal Research* 165, 189–216.
- Cottrell, E. & Kelley, K. A. (2011). The oxidation state of Fe in MORB glasses and the oxygen fugacity of the upper mantle. *Earth and Planetary Science Letters* **305**, 270–282.
- Danyushevsky, L. V. (2001). The effect of small amounts of H₂O on crystallisation of mid- ocean ridge and backarc basin

- magmas. *Journal of Volcanology and Geothermal Research* **110**, 265–280.
- Danyushevsky, L. V. & Plechov, P. (2011). Petrolog3: Integrated software for modeling crystallization processes. *Geochemistry, Geophysics, Geosystems* **12**, Q07021.
- Danyushevsky, L. V., Della-Pasqua, F. N. & Sokolov, S. (2000). Re-equilibration of melt inclusions trapped by magnesian olivine phenocrysts from subduction-related magmas: petrological implications. *Contributions to Mineralogy and Petrology* 138, 68–83.
- Danyushevsky, L. V., Leslie, R. A. J., Crawford, A. J. & Durance, P. (2004). Melt inclusions in primitive olivine phenocrysts: the role of localized reaction processes in the origin of anomalous compositions. *Journal of Petrology* 45, 2531–2553.
- Dasgupta, R., Hirschmann, M. M. & Smith, N. D. (2007). Partial melting experiments of peridotite + CO₂ at 3 GPa and genesis of alkalic ocean island basalts. *Journal of Petrology* **48**, 2093–2124.
- Demouchy, S. & Mackwell, S. (2006). Mechanisms of hydrogen incorporation and diffusion in iron-bearing olivine. *Physics and Chemistry of Minerals* **33**, 347–355.
- Dixon, J. E. (1997). Degassing of alkalic basalts. *American Mineralogist* **82**, 368–378.
- Dixon, J. E., Clague, D. A. & Stolper, E. M. (1991). Degassing history of water, sulfur, and carbon in submarine lavas from Kilauea Volcano, Hawaii. *Journal of Geology* 371–394.
- Dixon, J. E., Clague, D. A., Wallace, P. & Poreda, R. (1997). Volatiles in alkalic basalts from the North Arch Volcanic Field, Hawaii: Extensive degassing of deep submarine-erupted alkalic series lavas. *Journal of Petrology* 38, 911–939.
- Dixon, J. E., Leist, L., Langmuir, C. & Schilling, J.-G. (2002).
 Recycled dehydrated lithosphere observed in plume-influenced mid-ocean-ridge basalt. *Nature* 420, 385–389.
- Duan, X. (2014). A general model for predicting the solubility behavior of H₂O-CO₂ fluids in silicate melts over a wide range of pressure, temperature and compositions. *Geochimica et Cosmochimica Acta* **125**, 582–609.
- Eschenbacher, A. J. (1998). Open-system degassing of a fractionating, alkaline magma, Mount Erebus, Ross Island, Antarctica. Master's thesis. New Mexico Institute of Mining and Technology, http://www.ees.nmt.edu/outside/alumni/papers/1998t_eschenbacher_aj.pdf.
- Esser, R., Kyle, P. & McIntosh, W. (2004). ⁴⁰Ar/³⁹Ar dating of the eruptive history of Mount Erebus, Antarctica: volcano evolution. *Bulletin of Volcanology* **66**, 671–686.
- Faure, F. & Schiano, P. (2005). Experimental investigation of equilibration conditions during forsterite growth and melt inclusion formation. *Earth and Planetary Science Letters* 236, 882–898.
- Finotello, M., Nyblade, A., Julia, J., Wiens, D. & Anandakrishnan, S. (2011). Crustal V_p – V_s ratios and thickness for Ross Island and the Transantarctic Mountain front, Antarctica. *Geophysical Journal International* **185**, 85–92.
- Fodor, R. V. & Moore, R. B. (1994). Petrology of gabbroic xenoliths in 1960 Kilauea basalt: crystalline remnants of prior (1955) magmatism. *Bulletin of Volcanology* **56**, 62–74.
- Gaetani, G. A. & Grove, T. L. (1998). The influence of water on melting of mantle peridotite. *Contributions to Mineralogy* and Petrology 131, 323–346.
- Gaetani, G. A. & Watson, E. B. (2000). Open system behavior of olivine-hosted melt inclusions. *Earth and Planetary Science Letters* 183, 27–41.
- Gaetani, G. A., O'Leary, J. A., Shimizu, N., Bucholz, C. E. & Newville, M. (2012). Rapid reequilibration of H₂O and oxygen fugacity in olivine-hosted melt inclusions. *Geology* 40, 915–918.

- Gardner, J. E. (2012). Surface tension and bubble nucleation in phonolite magmas. *Geochimica et Cosmochimica Acta* 76, 93–102.
- Gerlach, T. M., McGee, K. A., Elias, T., Sutton, A. J. & Doukas, M. P. (2002). Carbon dioxide emission rate of Kilauea Volcano: Implications for primary magma and the summit reservoir. *Journal of Geophysical Research: Solid Earth* 107, 2189.
- Ghiorso, M. & Sack, R. (1995). Chemical mass transfer in magmatic processes IV. A revised and internally consistent thermodynamic model for the interpolation and extrapolation of liquid–solid equilibria in magmatic systems at elevated temperatures and pressures. *Contributions to Mineralogy and Petrology* 119, 197–212.
- Goldich, S. S., Treves, S. B., Suhr, N. H. & Stuckless, J. S. (1975). Geochemistry of the Cenozoic volcanic rocks of the Ross Island and vicinity, Antarctica. *Journal of Geology* 83, 415–435.
- Gonnermann, H. M. & Manga, M. (2005). Nonequilibrium magma degassing: Results from modeling of the ca. 1340 A.D. eruption of Mono Craters, California. Earth and Planetary Science Letters 238, 1–16.
- Grove, T. L. & Baker, M. B. (1984). Phase equilibrium controls on the tholeiitic versus calc- alkaline differentiation trends. *Journal of Geophysical Research: Solid Earth* 89, 3253–3274.
- Gudmundsson, A. (2006). How local stresses control magmachamber ruptures, dyke injections, and eruptions in composite volcanoes. *Earth-Science Reviews* **79**, 1–31.
- Gupta, S., Zhao, D. & Rai, S. S. (2009). Seismic imaging of the upper mantle under the Erebus hotspot in Antarctica. *Gondwana Research* **16**, 109–118.
- Hall, J., Wilson, T. & Henrys, S. (2007). Structure of the central Terror Rift, western Ross Sea, Antarctica. In: Cooper, A.K. & Raymond, C.R. (eds) Antarctica: A Keystone in a Changing World—Online Proceedings of the 10th International Symposium on Antarctic Earth Sciences. US Geological Survey Open-File Report 2007-1047, Research Paper 108.
- Harpel, C. J., Kyle, P. R. & Dunbar, N. W. (2008). Englacial tephrostratigraphy of Erebus volcano, Antarctica. *Journal of Volcanology and Geothermal Research* 177, 549–568.
- Hartley, M. E., Neave, D. A., Maclennan, J., Edmonds, M. & Thordarson, T. (2015). Diffusive over-hydration of olivinehosted melt inclusions. *Earth and Planetary Science Letters* 425, 168–178.
- Humphreys, M. C. S., Kearns, S. L. & Blundy, J. D. (2006). SIMS investigation of electron- beam damage to hydrous, rhyolitic glasses: Implications for melt inclusion analysis. *American Mineralogist* 91, 667–679.
- lacono-Marziano, G., Morizet, Y., Le Trong, E. & Gaillard, F. (2012). New experimental data and semi-empirical parameterization of H₂O-CO₂ solubility in mafic melts. *Geochimica et Cosmochimica Acta* **97**, 1–23.
- Iacovino, K., Oppenheimer, C., Scaillet, B. & Kyle, P. (2016). Storage and evolution of mafic and intermediate alkaline magmas beneath Ross Island, Antarctica. *Journal of Petrology* 57, 93–118.
- Iverson, N. A., Kyle, P. R., Dunbar, N. W., McIntosh, W. C. & Pearce, N. J. P. (2014). Eruptive history and magmatic stability of Erebus volcano, Antarctica: Insights from englacial tephra. Geochemistry, Geophysics, Geosystems 15, 4180–4202.
- Johnson, E. R., Wallace, P. J., Cashman, K. V., Granados, H. D. & Kent, A. J. R. (2008). Magmatic volatile contents and degassing-induced crystallization at Volcán Jorullo, Mexico: Implications for melt evolution and the plumbing systems of monogenetic volcanoes. *Earth and Planetary Science Letters* 269, 478–487.

- Kadik, A., Lukanin, O., Lebedev, Y. B. & Korovushkina, E. Y. (1972). Solubility of H₂O and CO₂ in granite and basalt melts at high pressures. *Geochemistry International* **9**, 1041–1050.
- Karlstrom, L., Dufek, J. & Manga, M. (2009). Organization of volcanic plumbing through magmatic lensing by magma chambers and volcanic loads. *Journal of Geophysical Research: Solid Earth* 114, B10204.
- Kent, A. J. R. (2008). Melt inclusions in basaltic and related volcanic rocks. In: Putirka, K. D. & Tepley, F. J., III (eds) Minerals, Inclusions and Volcanic Processes. Mineralogical Society of America and Geochemical Society, Reviews in Mineralogy and Geochemistry 69, 273–331.
- Kent, A. J. R., Stolper, E. M., Francis, D., Woodhead, J., Frei, R. & Eiler, J. (2004). Mantle heterogeneity during the formation of the North Atlantic Igneous Province: Constraints from trace element and Sr-Nd-Os-O isotope systematics of Baffin Island picrites. *Geochemistry, Geophysics, Geosystems* 5, Q11004.
- Koleszar, A. M., Saal, A. E., Hauri, E. H., Nagle, A. N., Liang, Y. & Kurz, M. D. (2009). The volatile contents of the Galapagos plume; evidence for H₂O and F open system behavior in melt inclusions. *Earth and Planetary Science Letters* **287**, 442–452.
- Kress, V. C. & Carmichael, I. S. E. (1991). The compressibility of silicate liquids containing Fe₂O₃ and the effect of composition, temperature, oxygen fugacity and pressure on their redox states. *Contributions to Mineralogy and Petrology* **108**, 82−92.
- Kyle, P. R. (1976). Geology, mineralogy and geochemistry of the late Cenozoic McMurdo volcanic group, Victoria Land, Antarctica. Ph.D. thesis, Victoria University of Wellington.
- Kyle, P. R. (1977). Mineralogy and glass chemistry of recent volcanic ejecta from Mt Erebus, Ross Island, Antarctica. New Zealand Journal of Geology and Geophysics 20, 1123–1146.
- Kyle, P. R. (1981a). The geological history of Hut Point Peninsula as indicated by Dry Valley Project holes 1, 2, and 3. In: McGinnis, L. D. (ed.) Dry Valley Drilling Project. Antarctic Research Series, American Geophysical Union 33, 427–445.
- Kyle, P. R. (1981b). Mineralogy and geochemistry of a basanite to phonolite sequence at Hut Point Peninsula, Antarctica, based on core from Dry Valley Drilling Project Drillholes 1, 2, and 3. *Journal of Petrology* 22, 451–500.
- Kyle, P. R. (1990a). Erebus Volcanic Province: Summary. In: LeMasurier, W. & Thompson, J. (eds) Volcanism of the Antarctic Plate and Southern Oceans. Antarctic Research Series, American Geophysical Union 48, 81–88.
- Kyle, P. R. (1990b). Hut Point Peninsula. In: LeMasurier, W. & Thompson, J. (eds) Volcanism of the Antarctic Plate and Southern Oceans. Antarctic Research Series, American Geophysical Union 48, 109–112.
- Kyle, P. R., Moore, J. A. & Thirlwall, M. F. (1992). Petrologic evolution of anorthoclase phonolite lavas at Mount Erebus, Ross Island, Antarctica. *Journal of Petrology* 33, 849–875.
- Larsen, L. M. & Pedersen, A. K. (2000). Processes in high-Mg, high-T magmas: evidence from olivine, chromite and glass in Palaeogene picrites from West Greenland. *Journal of Petrology* 41, 1071–1098.
- Lesne, P., Kohn, S. C., Blundy, J., Witham, F., Botcharnikov, R. E. & Behrens, H. (2011). Experimental simulation of closed-system degassing in the system basalt–H₂O–CO₂–S–Cl. *Journal of Petrology* **52**, 1737–1762.
- Liu, Y., Anderson, A., Wilson, C. N., Davis, A. & Steele, I. (2006). Mixing and differentiation in the Oruanui rhyolitic magma, Taupo, New Zealand: evidence from volatiles and trace

- elements in melt inclusions. *Contributions to Mineralogy and Petrology* **151**, 71–87.
- Lloyd, A. S., Plank, T., Ruprecht, P., Hauri, E. H. & Rose, W. (2013). Volatile loss from melt inclusions in pyroclasts of differing sizes. *Contributions to Mineralogy and Petrology* 165, 129–153.
- Lloyd, A. S., Ruprecht, P., Hauri, E. H., Rose, W., Gonnermann, H. M. & Plank, T. (2014). NanoSIMS results from olivinehosted melt embayments: Magma ascent rate during explosive basaltic eruptions. *Journal of Volcanology and Geothermal Research* 283, 1–18.
- Lowenstern, J. B. (1995). Applications of silicate-melt inclusions to the study of magmatic volatiles. In: Thompson, J.
 F. H. (ed.) Magmas, Fluids and Ore Deposits. Mineralogical Association of Canada, Short Course Series 23.71–99.
- Mackwell, S. J. & Kohlstedt, D. L. (1990). Diffusion of hydrogen in olivine: Implications for water in the mantle. *Journal of Geophysical Research: Solid Earth* **95**, 5079–5088.
- Maclennan, J. (2008). Concurrent mixing and cooling of melts under Iceland. *Journal of Petrology* **49**, 1931–1953.
- Mallmann, G., O'Neill, H., Berry, A., Norman, M., Eggins, S., Kamenetsky, V., Turner, S., Smith, I. & Ballhaus, C. (2011). The oxidation state of terrestrial basalts and its link with the mantle. *AGU Fall Meeting Abstracts*, 2551.
- Mandeville, C. W., Webster, J. D., Rutherford, M. J., Taylor, B. E., Timbal, A. & Faure, K. (2002). Determination of molar absorptivities for infrared absorption bands of H_2O in andesitic glasses. *American Mineralogist* **87**, 813–821.
- Mangan, M. & Sisson, T. (2000). Delayed, disequilibrium degassing in rhyolite magma: decompression experiments and implications for explosive volcanism. *Earth and Planetary Science Letters* **183**, 441–455.
- Marianelli, P., Sbrana, A., Métrich, N. & Cecchetti, A. (2005). The deep feeding system of Vesuvius involved in recent violent strombolian eruptions. *Geophysical Research Letters* 32, L02306.
- McKenzie, D. A. N. & O'Nions, R. K. (1991). Partial melt distributions from inversion of rare earth element concentrations. *Journal of Petrology* **32**, 1021–1091.
- Médard, E. & Grove, T. (2008). The effect of H₂O on the olivine liquidus of basaltic melts: experiments and thermodynamic models. *Contributions to Mineralogy and Petrology* **155**, 417–432.
- Metrich, N. & Clocchiatti, R. (1989). Melt inclusion investigation of the volatile behaviour in historic alkali basaltic magmas of Etna. *Bulletin of Volcanology* **51**, 185–198.
- Michael, P. (1995). Regionally distinctive sources of depleted MORB: Evidence from trace elements and H₂O. *Earth and Planetary Science Letters* **131**, 301–320.
- Mironov, N., Portnyagin, M., Botcharnikov, R., Gurenko, A., Hoernle, K. & Holtz, F. (2015). Quantification of the CO₂ budget and H₂O–CO₂ systematics in subduction-zone magmas through the experimental hydration of melt inclusions in olivine at high H₂O pressure. *Earth and Planetary Science Letters* **425**, 1–11.
- Miyashiro, A. (1978). Nature of alkalic volcanic rock series. *Contributions to Mineralogy and Petrology* **66**, 91–104.
- Moore, L. R., Gazel, E., Tuohy, R., Lloyd, A. S., Esposito, R., Steele-MacInnis, M., Hauri, E. H., Wallace, P. J., Plank, T. & Bodnar, R. J. (2015). Bubbles matter: An assessment of the contribution of vapor bubbles to melt inclusion volatile budgets. American Mineralogist 100, 806–823.
- Newcombe, M. E., Fabbrizio, A., Zhang, Y., Ma, C., Le Voyer, M., Guan, Y., Eiler, J. M., Saal, A. E. & Stolper, E. M. (2014). Chemical zonation in olivine-hosted melt inclusions. Contributions to Mineralogy and Petrology 168, 1030.

- Newman, S. & Lowenstern, J. B. (2002). VolatileCalc: a silicate melt–H₂O–CO₂ solution model written in Visual Basic for Excel. *Computers and Geosciences* **28**, 597–604.
- Oppenheimer, C., Moretti, R., Kyle, P. R., Eschenbacher, A., Lowenstern, J. B., Hervig, R. L. & Dunbar, N. W. (2011). Mantle to surface degassing of alkalic magmas at Erebus volcano, Antarctica. *Earth and Planetary Science Letters* 306, 261–271.
- Papale, P., Moretti, R. & Barbato, D. (2006). The compositional dependence of the saturation surface of $\rm H_2O + \rm CO_2$ fluids in silicate melts. *Chemical Geology* **229**, 78–95.
- Pichavant, M., Di Carlo, I., Rotolo, S., Scaillet, B., Burgisser, A., Le Gall, N. & Martel, C. (2013). Generation of CO₂-rich melts during basalt magma ascent and degassing. *Contributions to Mineralogy and Petrology* **166**, 545–561.
- Putirka, K. D., Perfit, M., Ryerson, F. J. & Jackson, M. G. (2007). Ambient and excess mantle temperatures, olivine thermometry, and active vs. passive upwelling. *Chemical Geology* 241, 177–206.
- Qin, Z. W., Lu, F. Q. & Anderson, A. T. (1992). Diffusive reequilibration of melt and fluid inclusions. *American Mineralogist* 77, 565–576.
- Riker, J. (2005). The 1859 Eruption of Mauna Loa Volcano, Hawai'i: Controls on the Development of Long Lava Channels. Master's thesis, University of Oregon, Eugene.
- Roberge, J., Delgado-Granados, H. & Wallace, P. J. (2009). Mafic magma recharge supplies high CO₂ and SO₂ gas fluxes from Popocatépetl volcano, Mexico. *Geology* 37, 107–110.
- Rocchi, S., Armienti, P. & Di Vincenzo, G. (2005). No plume, no rift magmatism in the West Antarctic Rift. In: Foulger, G. R., Anderson, D. L., Natland, J. H. & Presnall, D. C. (eds) *Plates, Plumes and Paradigms. Geological Society of America, Special Papers* 388, 435–447.
- Roedder, E. (1979). Origin and significance of magmatic inclusions. *Bulletin de Minéralogie* **102**, 487–510.
- Roggensack, K., Hervig, R. L., McKnight, S. B. & Williams, S. N. (1997). Explosive basaltic volcanism from Cerro Negro Volcano: Influence of volatiles on eruptive style. *Science* 277, 1639–1642.
- Rooney, T., Hart, W., Hall, C., Ayalew, D., Ghiorso, M., Hidalgo, P. & Yirgu, G. (2012). Peralkaline magma evolution and the tephra record in the Ethiopian Rift. *Contributions to Mineralogy and Petrology* **164**, 407–426.
- Ruprecht, P. & Plank, T. (2013). Feeding andesitic eruptions with a high-speed connection from the mantle. *Nature* **500**, 69–72
- Ruprecht, P., Plank, T. & Lloyd, A. (2010). Melt inclusion reequilibration with complex shapes. *AGU Fall Meeting Abstracts* V53C–2265.
- Rust, A. C., Cashman, K. V. & Wallace, P. J. (2004). Magma degassing buffered by vapor flow through brecciated conduit margins. *Geology* 32, 349–352.
- Rutherford, M. J. & Gardner, J. E. (1999). Rates of magma ascent. In: Sigurdsson, H., Houghton, B., Rymer, I., Stix, J. & McNutt, S. (eds) *Encyclopedia of Volcanoes*. London: Academic Press, pp. 207–218.
- Sarda, P. & Graham, D. (1990). Mid-ocean ridge popping rocks: implications for degassing at ridge crests. *Earth and Planetary Science Letters* **97**, 268–289.
- Schiano, P., Clocchiatti, R., Bourdon, B., Burton, K. W. & Thellier, B. (2000). The composition of melt inclusions in minerals at the garnet–spinel transition zone. *Earth and Planetary Science Letters* **174**, 375–383.
- Sims, K. W. W., Blichert-Toft, J., Kyle, P. R., Pichat, S., Gauthier, P. J., Blusztajn, J., Kelly, P., Ball, L. & Layne, G. (2008). A Sr, Nd, Hf, and Pb isotope perspective on the genesis and long-

- term evolution of alkaline magmas from Erebus volcano, Antarctica. *Journal of Volcanology and Geothermal Research* **177**, 606–618.
- Sims, K.W.W., Pichat, S., Reagan, M. K., Kyle, P. R., Dulaiova, H., Dunbar, N., Prytulak, J., Sawyer, G., Layne, G., Blichert-Toft, J., Gauthier, P. J., Charrette, M. A. & Elliott, T. R. (2013). On the timescales of magma genesis, melt evolution, crystal growth rates and magma degassing in the Erebus volcano magmatic system using the ²³⁸U, ²³⁵U- and ²³²Th-decay series. *Journal of Petrology* **54**, 235–271.
- Sparks, R. S. J., Barclay, J., Jaupart, C., Mader, H. M. & Phillips, J. C. (1994). Physical aspects of magma degassing; 1, Experimental and theoretical constraints on vesiculation. In: Carroll, M. R. & Holloway, J. R. (eds) Volatiles in Magmas. Mineralogical Society of America, Reviews in Mineralogy 30, 413–445.
- Spilliaert, N., Allard, P., Métrich, N. & Sobolev, A. V. (2006). Melt inclusion record of the conditions of ascent, degassing, and extrusion of volatile-rich alkali basalt during the powerful 2002 flank eruption of Mount Etna (Italy). *Journal of Geophysical Research: Solid Earth* 111, B04203.
- Steele-MacInnis, M., Esposito, R. & Bodnar, R. J. (2011). Thermodynamic model for the effect of post-entrapment crystallization on the H₂O-CO₂ systematics of vapor-saturated, silicate melt inclusions. *Journal of Petrology* **52**, 2461–2482.
- Stuckless, J. S., Miesch, A. T., Goldich, S. S. & Weiblen, P. W. (1981). A Q mode factor model for the petrogenesis of the volcanic rocks from Ross Island and vicinity, Antarctica. In: McGinnis, L.D. (ed.) Dry Valley Drilling Project. Antarctic Research Series, American Geophysical Union 33, 257–280.
- Sun, S. & Hanson, G. (1975). Origin of Ross Island basanitoids and limitations upon the heterogeneity of mantle sources for alkali basalts and nephelinites. *Contributions to Mineralogy and Petrology* **52**, 77–106.
- Sun, S. & McDonough, W. F. (1989). Chemical and isotopic systematics of oceanic basalts: implications for mantle composition and processes. In: Saunders, A. D. & Norry, M. J. (eds) Magmatism in the Ocean Basins. Geological Society, London, Special Publications 42, 313–345.
- Tait, S. (1992). Selective preservation of melt inclusions in igneous phenocrysts. American Mineralogist 77, 146–155.
- Vigouroux, N., Wallace, P. J. & Kent, A. J. R. (2008). Volatiles in high-K magmas from the western Trans-Mexican Volcanic

- Belt: Evidence for fluid fluxing and extreme enrichment of the mantle wedge by subduction processes. *Journal of Petrology* **49**, 1589–1618.
- Wallace, P. J. (2005). Volatiles in subduction zone magmas: concentrations and fluxes based on melt inclusion and volcanic gas data. *Journal of Volcanology and Geothermal Research* 140, 217–240.
- Wallace, P. J. & Anderson, A. T., Jr (1998). Effects of eruption and lava drainback on the H_2O contents of basaltic magmas at Kilauea Volcano. *Bulletin of Volcanology* **59**, 327–344.
- Wallace, P. J., Kamenetsky, V. S. & Cervantes, P. (2015). Melt inclusion CO₂ contents, pressures of olivine crystallization, and the problem of shrinkage bubbles. *American Mineralogist* **100**, 787–794.
- Watson, E. B. (1994). Diffusion in volatile-bearing magmas. In: Carroll, M. R. & Holloway, J. R. (eds) Volatiles in Magmas. Mineralogical Society of America, Reviews in Mineralogy 30, 371–411.
- Watson, T., Nyblade, A., Wiens, D. A., Anandakrishnan, S., Benoit, M., Shore, P. J., Voigt, D. & VanDecar, J. (2006). P and S velocity structure of the upper mantle beneath the Transantarctic Mountains, East Antarctic craton, and Ross Sea from travel time tomography. *Geochemistry, Geophysics, Geosystems* 7, Q07005.
- Welsch, B., Hammer, J. & Hellebrand, E. (2014). Phosphorus zoning reveals dendritic architecture of olivine. *Geology* 42, 867–870.
- Witham, F. (2011). Conduit convection, magma mixing, and melt inclusion trends at persistently degassing volcanoes. *Earth and Planetary Science Letters* **301**, 345–352.
- Wright, A. C. & Kyle, P. R. (1990a). Mount Bird. In: LeMasurier, W. & Thompson, J. (eds) Volcanism of the Antarctic Plate and Southern Oceans. Antarctic Research Series, American Geophysical Union 48, 97–98.
- Wright, A. C. & Kyle, P. R. (1990b). Mount Terror. In: LeMasurier, W. & Thompson, J. (eds) *Volcanism of the Antarctic Plate and Southern Oceans. Antarctic Research Series, American Geophysical Union* **48**, 99–102.
- Wysoczanski, R. & Tani, K. (2006). Spectroscopic FTIR imaging of water species in silicic volcanic glasses and melt inclusions: An example from the Izu–Bonin arc. *Journal of Volcanology and Geothermal Research* **156**, 302–314.
- Yoshimura, S. & Nakamura, M. (2010). Chemically driven growth and resorption of bubbles in a multivolatile magmatic system. *Chemical Geology* **276**, 18–28.